Deformation mechanism in ultrafine-grained metals with an emphasis on the Hall-Petch relationship and strain rate sensitivity

Roberto B. Figueiredo[1,*], Terence G. Langdon[2]

[1] Metallurgical and Materials Engineering Department, Universidade Federal de Minas Gerais, Belo Horizonte, MG 31270-901, Brazil

[2] Materials Research Group, Department of Mechanical Engineering, University of Southampton, Southampton SO17 1BJ, U.K.

Abstract

Ultrafine-grained materials display almost no strain hardening, an enhanced strain rate sensitivity and grain boundary offsets during plastic deformation. It is expected that dislocation climb is active in order to enable prompt recovery. The present analysis proposes a deformation mechanism that includes these effects and follows from the mechanism for high temperature grain boundary sliding. This mechanism predicts the relationship between strain rate, flow stress, grain size, temperature and basic material properties such as the Burgers vector modulus, the shear modulus and the grain boundary diffusion coefficient. The model may be used to estimate the final grain size achieved by severe plastic deformation and the strain rate sensitivity. An analysis shows that the predicted behavior agrees with the data from multiple experimental investigations and provides a good estimate of the Hall-Petch slope for different materials which includes breakdown and inverse Hall-Petch behavior under some conditions. The incorporation of a threshold stress provides an opportunity to predict the relationship between flow stress and grain size for a broad range of grain sizes, strain rates and temperatures. An excellent agreement is observed between the predictions of the model and experimental data for Al, Cu, Fe (α), Fe(γ), Mg, Ni, Ti and Zn.

Keywords: deformation mechanisms; grain boundary sliding; Hall-Petch relationship; ultrafine grains.

*Corresponding author: figueiredo@demet.ufmg.br

1. Introduction to materials exhibiting grain refinement

The deformation behavior of coarse-grained metallic materials is well understood [1]. The strain hardening due to an accumulation of dislocations plays a major role in the low temperature deformation of metals. For example, it is now well established that f.c.c. metals display multiple stages of hardening which are associated with the accumulation and recovery of dislocations. Initially, stage I is characterized by the easy glide of dislocations at relatively low stresses in single crystals [1]. This is followed by a rapid linear hardening in stage II where both screw and edge dislocations are accumulated. Stage III is characterized by recovery of screw dislocations through cross-slip and then an accumulation of edge dislocations takes place in stage IV and there is recovery of edge dislocations through climb in stage V [2]. Nevertheless, the deformation mechanisms of severely deformed ultrafine-grained and nanocrystalline metals, in which there is no anticipated dislocation accumulation, remains a scientific area where there are numerous uncertainties.

This topic has attracted significant attention in recent decades due to the development of various processing techniques which provide the capability of producing samples with exceptionally fine grains. Thus, in principle the grain sizes of metallic samples are reduced through the use of thermo-mechanical processing but these conventional procedures are not capable of producing grain sizes smaller than a few micrometers. Alternative procedures are based on two different and distinct methods for producing metals with very small grain sizes [3]. The first procedure is the so-called “bottom-up” approach in which materials are fabricated through the compaction of individual atoms as in inert gas condensation, electrodeposition, chemical and physical deposition or cryomilling with hot isostatic pressing. These methods effectively produce very small grain sizes but the samples are generally extremely small, typically of use only in miniature electronic applications and they contain some residual porosity. The second procedure is the so-called “top-down” approach where a solid fully-dense bulk material is processed to produce grain refinement through heavy straining and/or shock loading. These methods are capable of producing grain refinement in a very wide range of materials including the production of ultrafine grains with grain sizes within the limits of 100-1000 nm and, under some conditions, producing true nanostructured materials with grain sizes of <100 nm [4]. A recent review examined some of the mechanisms that are proposed to explain the deformation behavior of materials with very small grain sizes [5]. However, most of these mechanisms were developed to explain the behavior for grain sizes of less than 100 nm that are produced using “bottom-up” techniques. This means the small grains were not introduced in bulk samples and there will be varying degrees of sample purity and sample porosity with a consequent scatter between different sets of experimental data.

By contrast, the “top-down” approach relies specifically on the imposition of severe plastic deformation (SPD) techniques in which the sample is deformed without incurring any significant changes in the overall dimensions of the work-pieces [6]. By refining the grain structure of bulk specimens, there is a direct control over the sample purity and materials are produced in a fully-dense state without any inherent porosity thereby leading to less scatter in the experimental data. The grain sizes of samples produced using SPD are often in the ultrafine range of 100 - 1000 nm and it is reasonable to anticipate that the deformation behavior of these materials may differ from that observed in their nanocrystalline counterparts. For example, most of the experimental data shows that materials processed by SPD exhibit strengthening at room temperature as the grain size decreases. Although this is consistent with the well-established Hall-Petch (H-P) effect [7, 8], there are reports of an inverse Hall-Petch effect in some nanocrystalline materials

[9, 10]. Furthermore, most research on the deformation behavior of ultrafine-grained materials has been empirical but some effects are now widely accepted. It is known, for example, that these materials usually display high strength, no significant strain hardening, there is a stable or saturation grain size produced after sufficient SPD processing and the processed grain size decreases with increasing alloying content [11] and decreasing processing temperature [12]. Also, the deformation mechanism of these materials is temperature-dependent and therefore thermally-activated. The latter effect is reflected in an enhanced strain rate sensitivity which may be used in order to stabilize the plastic deformation and thereby increase the elongation in tension. Therefore, there appears to be a clear opportunity for developing materials having both high strength and reasonable ductility.

Although these effects have been reported widely, no clear explanation is available at present. For example, the room temperature enhanced strain rate sensitivity observed in ultrafine-grained materials has been attributed to an enhanced contribution of grain boundary sliding to the deformation but it is not clear whether the experimental data are consistent with the models for high temperature grain boundary sliding. Also, there is no clear discussion on whether the ultrafine-grained materials follow the same Hall-Petch trend observed in their coarse-grained counterparts. A reduced H-P slope has been reported [13] but also an increased slope [14] and even an inverse H-P behavior in pure Mg [15]. Furthermore, it is known that the minimum grain size attained after SPD processing is related to various physical parameters including the stable subgrain size [16, 17] but this stable subgrain size depends on the applied stress which is often not adequately incorporated in any model. It is worth noting that an empirical analysis of the minimum stable grain size in pure metals processed by SPD revealed many trends, including a reduction in grain size both with increasing activation energy for self-diffusion and with hardness and almost no dependence on stacking fault energy [18]. In practice, an understanding of the deformation mechanism of ultrafine-grained materials will provide important information on the enhanced strain rate sensitivity of these materials, the relationship between grain size and strength and also the relationship between the straining introduced in SPD processing and the minimum grain size. Accordingly, the overall objective of this report is to examine these relationships for a wide range of experimental data reported in the literature.

2. Fundamental principles in examining the flow processes in ultrafine-grained materials

The deformation mechanism proposed in this report follows directly from the model developed earlier for high temperature grain boundary sliding [19] and it is supported by two widely accepted effects. First, ultrafine-grained materials generally display little or no strain hardening which suggests that the rate of defect generation during deformation is approximately equal to the rate of recovery. In practice, the balance between defect generation and recovery at the end of stage V of the conventional model for strain hardening has been associated with the annihilation of edge dislocations through climb [2]. Therefore, dislocation climb must be activated in order to prevent defect accumulation in ultrafine-grained metals. High stresses can promote the non-conservative climb of jogged dislocations leading to the creation of point defects where this is in agreement with the observations of high densities of vacancies in ultrafine-grained metals processed by SPD [20]. Second, it is now readily accepted that grain boundary sliding plays a role in the deformation of ultrafine-grained metals as supported by experimental evidence for the occurrence of grain boundary offsets after the room temperature plastic deformation of several materials including aluminum [21], copper [22] and magnesium [15, 23]. Although the present model is derived to describe the deformation behavior of ultrafine-grained metals, it will be demonstrated that it agrees also with experimental data reported in materials with grain sizes as small as ~20 nm and, in addition, it provides an estimate of the yield stress of coarse-grained metals when no substructure is present [24].

In order to develop this approach, it is first necessary to define the principles of processing using SPD techniques. Basically, there are numerous procedures for processing by SPD but these approaches necessarily exclude conventional procedures such as extrusion or rolling where the overall dimensions of the work-piece are reduced by processing. Instead, it is necessary to consider special procedures that have been developed specifically for imposing high strains without any significant sample deformation and the two main and most important methods are equal-channel angular pressing (ECAP) and high-pressure torsion (HPT) [25]. In ECAP, the sample is in the form of a rod or bar and it is pressed through a die constrained within a channel which is bent through an abrupt angle near the center of the die [26]. Typically, ECAP processing will produce a fully-dense ultrafine-grained material but in some materials the grains may be slightly larger or smaller than those required for the ultrafine range. In HPT, the sample is generally in the form of a fairly thin disk and it is held within an HPT facility between two massive anvils and then subjected to a high applied pressure and concurrent torsional straining [27]. Using this procedure, the grains are often within the range for ultrafine-grained metals but in many samples it is possible to produce materials having grain sizes within the true nanometer range.

3. Outline of the principles of the model

The proposed mechanism follows from the model developed earlier for grain boundary sliding at high temperatures [19]. Thus, extrinsic dislocations glide along grain boundaries and this produces dislocation pile-ups at obstacles such as triple junctions. The stress at the head of the pile-up builds and then activates a dislocation source on a different slip system in the blocking grain. These dislocations glide through the opposing grain, pile up at the opposite grain boundary and then climb and are absorbed into the boundary. The basic features of the model are illustrated schematically in Fig. 1.

In practice, the stress at the head of the pile-up, σ_p, increases proportionally to its length, L, since

$$\sigma_p \cong \frac{2L\tau^2}{Gb} \qquad (1)$$

where τ is the shear stress acting on the slip plane in the direction of the Burgers vector, b, and G is the shear modulus. The climb velocity, v_c, is controlled by the rate of diffusion of vacancies and is given by [28]:

$$v_c = \frac{D}{h}\left[exp\left(\frac{\sigma_p b^3}{kT}\right) - 1\right] \qquad (2)$$

where h is the climb distance, k is Boltzmann's constant, T is the absolute temperature and, since the dislocations climb along the grain boundary in Fig. 1, it is reasonable to take D as the grain boundary diffusion coefficient. This latter assumption is supported by, for example, experimental measurements of the activation energy for deformation of HPT-processed aluminum [29]. The time required for the dislocation to climb through a distance h is h/v_c and the sliding rate, $\dot{\gamma}$, is b/t, where t is the time. Therefore, the overall sliding rate, $\dot{\varepsilon}$, is inversely proportional to the grain size, d, and is given by $\dot{\gamma}/\sqrt{3}\,d$.

The earlier analysis [19] was focused on high temperature grain boundary sliding and therefore made use of a reasonable approximation of the form:

$$exp\left(\frac{\sigma_p b^3}{kT}\right) - 1 = \frac{\sigma_p b^3}{kT} \qquad (3)$$

for conditions where $\sigma_p b^3 \ll kT$. This approximation was valid because the stresses are low in high temperature creep and the rapid diffusion at high temperatures leads to a negligible supersaturation of vacancies. However, in low temperature deformation the stresses are significantly higher and there will be a supersaturation of vacancies so that the approximation in eq. (3) is no longer valid. Thus, considering $\tau = \sigma/\sqrt{3}$, the rate of deformation is given by:

$$\dot{\varepsilon} = \frac{bD_{gb}}{\sqrt{3}dh^2}\left[exp\left(\frac{2L\sigma^2 b^2}{\sqrt{3}GkT}\right) - 1\right] \quad (4)$$

It should be noted that eq. (4) is valid when dislocations glide through a grain and reach the opposite grain boundary. Therefore, it is valid when no substructure, dislocation cell walls or subgrain boundaries are present and a steady-state is expected under conditions where the grain size is sufficiently small to prevent the formation of subgrains.

In practice, the average subgrain size, λ, varies inversely with the applied stress and the following relationship is applicable for all crystalline materials including metals [30], ceramics [31] and geological materials [32, 33]:

$$\frac{\lambda}{b} = \zeta\left(\frac{G}{\sigma}\right) \quad (5)$$

where ζ is a constant having a value approximately equal to 20. It is known that the grain size achieved in SPD processing is comparable to the subgrain size and subgrains are not present within the grains produced by SPD. Therefore, the assumption of dislocations gliding through the grain without intersecting a subgrain boundary is reasonable for materials processed by SPD.

Careful inspection of the deformation rate given by eq. (4) shows that there are basically three parameters related to the structural length: these are the grain size, d, the climb distance, h, and the pile-up length, L. In practice, these various parameters are mutually proportional since the grain size affects the pile-up length and the climb distance. In the earlier analysis [19] it was assumed that $L \approx l$, $h \approx 0.3l$ and $d \approx 1.7l$ where l is the mean linear intercept grain size. Making the same assumption for the present model, and considering the grain boundary width, δ, as $2b$, eq. (4) becomes

$$\dot{\varepsilon} \approx \frac{10\delta D_{gb}}{d^3}\left[exp\left(\frac{2d\sigma^2 b^2}{3GkT}\right) - 1\right] \tag{6}$$

It follows from eq. (6) that the grain size, and therefore the occurrence of grain refinement, affects the deformation rate in opposing ways. It is anticipated that decreasing the grain size increases the total contribution of the rate of grain boundary shear to the overall deformation. However, decreasing the grain size will also reduce the average climb distance. Both of these effects will increase the deformation rate through eq. (6) but in practice decreasing the grain size reduces the pile-up length and this in turn reduces the stress concentration at the head of the pile-up and thereby reduces the deformation rate.

4. A comparison with experimental data to validate the model

4.1. Stress vs. grain size

In order to evaluate the effect of grain size in the deformation mechanism, it is important to plot the relationship between the flow stress and the grain size. Thus, eq. (6) can be transformed to:

$$\sigma \approx \sqrt{\frac{3GkT}{2db^2} ln\left(\frac{\dot{\varepsilon}d^3}{10\delta D_{gb}} + 1\right)} \tag{7}$$

The model predicts that the strain rate and the flow stress will be a function of the temperature, grain size, shear modulus, Burgers vector modulus and grain boundary diffusion coefficient. The last three parameters are fundamental characteristics for any selected material and the individual values for a range of metals are summarized in Table 1 [34] where D_0 is the frequency factor in the diffusion coefficient and Q_{gb} is the activation energy for grain boundary diffusion. For convenience, the shear modulus of each metal was expressed in the conventional form as [31]

$$G = G_0 - (\Delta G)T \tag{8}$$

where G_0 is the value of the shear modulus obtained by a direct extrapolation from high temperatures to absolute zero and ΔG is the variation in shear modulus per degree Kelvin.

Figure 2 shows a plot of stress vs. grain size for room temperature (300 K) deformation of aluminum, copper, iron and nickel tested at a strain rate of 10^{-3} s^{-1} where each solid line is the prediction of the model for the various four metals. The strain rate of 10^{-3} s^{-1} was selected because it is representative for quasi-static mechanical testing but in practice it is noted that at room temperature the strain rate is of only minor significance in the relationship between stress and grain size for the deformation of materials having high melting points. Superimposed in Fig. 2 are experimental data taken from reports for Al [35-41], Cu [18, 22, 42-51], Fe [52-58] and Ni [14, 59-62] where a relationship between flow stress, σ, and hardness, H, of $\sigma = H/3$ [63] was used where appropriate.

The agreement between the model and the experimental data in Fig. 2 is exceptionally good despite the inherent uncertainties associated with experimental measurements of grain size and flow stress. Both the model and the experimental data predict an increase in flow stress with decreasing grain size but the model also predicts a change in slope and a breakdown or inverse behavior in aluminum at grain sizes of the order of tens of nanometers. This breakdown is not predicted for the other materials with higher melting temperatures, at least for grain sizes larger than 10 nm. In fact, experiments show there is consistent strengthening by grain refinement in iron with different purities even with grain sizes as small as ~20 nm [57]. It is important to note also that the model predicts an almost linear relationship on a double-logarithmic scale between σ and d with a slope of ~0.5 for all four metals except only for aluminum when the grain size is truly nanocrystalline. This behavior is similar to the Hall-Petch relationship in coarse-grained materials and it shows that, at least for these materials at this temperature and strain rate, the length of the dislocation pile-up plays a major role in controlling the flow stress.

4.2 Maximum grain size for steady-state deformation and the grain sizes achieved in SPD processing.

Although Fig. 2 shows good agreement between the model and experimental data for grain sizes >1 μm, a steady-state deformation in which the rate of defect generation is balanced by defect recovery requires that the formation of a subgrain structure is prevented. Therefore, any prediction of the present model for materials where the grain size is larger than the subgrain size is valid only for the yield stress when no substructure is present. However, no significant strain hardening is expected during the deformation of materials with grain sizes smaller than the subgrain size and therefore the present model predicts the steady-state behavior.

It is known that plastic deformation during SPD processing leads to an accumulation of dislocations in cells which evolve into subgrains having low-angle boundaries and then finally into grains having high-angle boundaries. As the subgrain size decreases with increasing applied stress, the subgrain size will decrease during processing in materials which undergo strain hardening but a stable subgrain size may be achieved when the strain hardening capability is exhausted. Thus, it is expected that processing by SPD will refine the grain structure until reaching the stable subgrain size and this condition corresponds to the present model becoming the rate-controlling deformation mechanism. It follows that it is possible for any material to estimate the stable grain size, or the saturation grain size, by equating the flow stress predicted by the present model with the relevant prediction for the subgrain size. Any grain size larger than this value would induce the formation of a subgrain structure which is associated with more dislocation accumulation and hardening. It is concluded from this analysis that only grains having sizes equal to or smaller than this prediction would fail to develop any subgrains.

In order to illustrate this conclusion, Fig. 3 shows the predicted flow stress at room temperature plotted as solid lines as a function of grain size for Al, Cu, Fe and Mg. Specifically, a strain-rate of 10^{-1} s^{-1} was used for this prediction since this is within the range of the expected strain rate at the edge of an HPT disk of 10 mm diameter and 0.8 mm thickness processed at a rotation rate of 0.2 rpm. The predicted relationship between the flow stresses and the subgrain sizes are also plotted using dashed lines for each material. Finally, the predicted maximum stable grain sizes, denoted as d_{stable}, are highlighted by the arrows which mark the intercepts between the solid and dashed lines for the four different materials. According to this approach, the maximum stable grain sizes are ~0.7 μm in Mg, ~0.7 μm in Al, ~0.4 μm in Cu and ~0.3 μm in Fe, respectively.

The values estimated using this approach for the maximum stable grain sizes agree well with experimental reports of grain sizes of ~0.5 – 1.0 μm in Mg [23, 64], ~0.6 – 1.2 μm in Al [37, 65], ~0.4 μm in Cu [66] and ~0.25 μm in Fe [53]. It is worth noting that the grain sizes in the plot in Fig. 3 correspond to the spatial grain size and this is equal to 1.74 × the mean linear intercept grain size [67] so that it is generally larger than the grain sizes measured experimentally. It is important also to note that this prediction of stable grain size corresponds to an upper bound limit of the grain size produced in HPT processing. In practice, many additional effects may induce further grain refinement such as the shear distortions of grains and the inherent flow patterns in the HPT samples [68-74], the presence of any minor misalignment between the massive upper and lower anvils [75-77] and/or the inherent roughness associated with the anvil surfaces [78].

It follows from this analysis that the stable grain size will be dependent upon the level of the flow stress during severe plastic deformation. Thus, increasing the flow stress of the material through alloying is expected to decrease the stable grain size as demonstrated in experimental observations [11]. Also, the coefficient of grain boundary diffusion plays a role in the predicted flow stress and it was noted that the hydrostatic pressure during HPT processing can increase the activation energy for self-diffusion in iron by up to ~30% [54]. Hence, assuming a similar effect for the grain boundary diffusion coefficient, it is expected that increasing the hydrostatic pressure will increase the flow stress during processing and thereby reduce the stable grain size. By contrast, the non-conservative climb of jogs may increase the vacancy concentration and this will accelerate the diffusion processes. An excess volume has been reported in metallic materials processed by HPT [79] and a reduced activation energy for deformation after HPT processing was reported in Al-Zn [29] and pure Mg [23]. Therefore, it is reasonable to anticipate there is some level of uncertainty concerning the appropriate diffusion coefficient and hence the associated flow stress during HPT processing.

It is important to note also that the prediction of the stable grain size during processing by HPT is also affected by the processing temperature. This is illustrated in Fig. 4 which shows, as a function of grain size, the predictions for the flow stress for copper at a strain rate of 10^{-1} s^{-1} at four separate temperatures from 100 to 473 K. As expected, an increase in temperature leads to a decrease in the predicted flow stress and, as shown by the dashed lines for the subgrain sizes and the predicted values for d_{stable}, it also leads to an increase in the stable grain size. This is in agreement with experimental observations of an increase in the final grain size of copper processed by HPT with increasing processing temperature, where there were reported grain sizes of ~0.4, ~0.6 and ~0.8 µm after HPT processing at 298, 393 and 473 K, respectively [66]. A decrease in grain size was also reported in copper processed at 100 K where the experimental grain size was ~73 nm [36] which is about four times smaller than the maximum stable grain size predicted by the present analysis.

4.3 *The inverse Hall-Petch effect*

The approach developed so far shows that the model predicts a trend of increasing stress with decreasing grain size within the ultrafine-grained range. Nevertheless, in practice there are clear reports of the opposite behavior in some materials processed by HPT. For example, an inverse Hall-Petch behavior was reported in pure magnesium [15, 23, 80] for grain sizes smaller than a few microns where this effect was observed at strain rates lower than ~10^{-2} s^{-1} and it was associated with a reduced activation energy of ~75 kJ/mol [15, 23]. As noted earlier, a reduced activation energy for grain boundary diffusion was observed in some materials processed by SPD [79] and this was associated with an excess free volume and the non-equilibrium nature of the high-energy grain boundaries which contained extrinsic dislocations [79, 81-83]. Figure 5 shows, as represented by the solid lines, a plot of the predicted stress versus grain size for pure magnesium at the two low strain rates of 10^{-5} and 10^{-3} s^{-1} considering an activation energy for grain boundary diffusion of Q_{gb} = 75 kJ/mol. Experimental datum points determined from tensile and compression tests [15, 23, 80, 84] are also included in Fig. 5 where the slower and faster strain rates are shown by the solid and open points, respectively. It is apparent that the model correctly predicts an inverse Hall-Petch behavior under these testing conditions and this is consistent with the experimental data.

Inspection of Fig. 5 shows that some of the experimental points lie at grain sizes which are larger than the predicted subgrain size. This means that substructure will build up during deformation under these conditions and this will prevent the steady-state operation of the proposed deformation mechanism. It is interesting to note that these points at larger grain sizes display higher flow stresses than predicted by the model and the experimentally observed softening takes place only for specimens where the grain sizes are in the range of the subgrain size or smaller. Therefore, the drop in flow stress at grain sizes smaller than the subgrain size is additional supporting evidence that different deformation mechanisms are operational in the regions above and below the subgrain size.

The present model also predicts an inverse Hall-Petch behavior in zinc at room temperature for grain sizes smaller than ~1 μm but with the transition grain size dependent on the strain rate. In practice, it is difficult to evaluate this prediction using experimental results available for pure zinc because the metal undergoes grain growth at room temperature and this is similar to other low melting point metals [85]. By contrast, grain growth is limited in Zn-Al alloys due to the presence of the Al phase and therefore Fig. 6 shows, for a strain rate of 10^{-4} s^{-1} and temperature of 300 K, a plot of stress against grain size for pure Zn. Also included in Fig. 6 as a dashed line are the predictions of the model based on the limiting grain size together with experimental points for the Zn-22% Al eutectoid alloy tested under these conditions where the stress was estimated as Hv/3 and Hv is the reported Vickers microhardness [86]. Thus, there is a prediction of grain refinement softening in pure Zn and this is consistent with experimental data reported, under the same conditions of temperature and strain rate, for the Zn-22% Al alloy.

4.4 Predictions for the strain rate sensitivity

It is now well established that an enhanced strain rate sensitivity is advantageous for materials processed by severe plastic deformation. Thus, early reports showed that pure copper [46, 87] and pure titanium [87], processed by ECAP and HPT, respectively, both exhibited high elongations in tension due to their increased values for the strain rate sensitivity. The present model predicts this effect.

Thus, Fig. 7 shows the predicted strain rate sensitivity, m, at room temperature for copper with grain sizes from 0.1 to 1.0 μm plotted as a function of stress. A high strain rate sensitivity of 0.5 is predicted at low stresses which agrees with the predicted value for high temperature grain boundary sliding but this value decreases with increasing stress. These plots show that the occurrence of grain refinement displaces the curves and thereby extends the region of high strain rate sensitivity to higher values of stresses. This means that the refining of grains by SPD will increase the measured value of *m*. The values of *m* reported from experiments for grain sizes of ~0.3 μm [46] and ~0.1 μm [87] are plotted in Fig. 7 as a function of the stresses at which these values were recorded and this demonstrates very good agreement with the theoretical predictions.

The model predicts that the strain rate sensitivity also increases with increasing temperature. Thus, provided the grain size is stable, there will be a higher strain rate sensitivity at higher temperatures leading ultimately to values of $m \approx 0.5$ which are associated with the occurrence of conventional superplasticity [88].

The model also predicts that the increase in room temperature strain rate sensitivity due to grain refinement is more evident in materials having lower melting temperatures such as aluminum, magnesium and zinc. In fact, strain rate sensitivities of 0.2 and larger have been reported in these materials [23, 89-91] and this is attributed to higher grain boundary diffusion coefficients and, consequently, larger contributions of diffusion to the deformation.

Figure 8 shows plots of stress versus strain rate at 300 K for (a) Zn and (b) Al together with experimental data [29, 91] where the prediction for zinc is compared to results for the Zn-22% Al alloy due to the occurrence of grain growth in pure zinc at room temperature.

Inspection of Fig. 8(a) shows there is excellent agreement between the model and the experimental results both in terms of the level of the flow stress and the slope of the curve for Zn. Thus, a strain rate sensitivity in the range of ~0.2 – 0.3 is predicted by the model for strain rates in the range of $10^{-4} - 10^{-3}$ s^{-1} and this is consistent with the experimental results where there was a value of $m \approx 0.226$ [91].

In Fig. 8(b) there is also a good agreement between the level of the flow stress and the predicted strain rate sensitivity of $m \approx 0.03$ with experimental data for pure aluminum having a grain size of ~1.2 μm where the experiments revealed an activation energy of ~87 kJ/mol during the testing of this material [29]. This activation energy is close to the anticipated value of ~84 kJ/mol for grain boundary diffusion in aluminum which supports the assumption in the present model that grain boundary diffusion is the rate-controlling diffusion mechanism. Figure 8(b) shows also experimental data reported for an Al-30% Zn alloy with a finer grain size of ~0.38 μm where there was a reduced activation energy of ~65 kJ/mol [29]. Again both the finer grain size and the reduced activation energy tend to increase the slope of the stress versus strain rate curves in the present model and there is again an excellent agreement between the predictions of the model and the experimental data. This increased slope is associated with an increased strain rate sensitivity and the model specifically predicts a value of m in the range of ~0.3 – 0.1 in the strain rate range of $10^{-4} - 10^{-2}$ s^{-1} where the experimental measurements give a value of $m \approx 0.22$ [29].

Additionally, a recent report documented a further grain refinement to a value of ~0.28 μm in a similar Al-30% Zn alloy after larger numbers of turns in HPT processing [89]. According to the predictions of the present model, this additional decrease in grain size will increase the strain rate sensitivity to ~0.36 at a strain rate of 10^{-4} s^{-1} and this is in good agreement with experiments which revealed a strain rate sensitivity of ~0.41 in the vicinity of this strain rate [89]. It is important to note also that this remarkable increase in m led to a superplastic elongation of >400% at room temperature in this material [89] and this is similar to the report of a tensile elongation of 440% in an Mg-8% Li alloy at room temperature when the strain rate sensitivity was $m \approx 0.37$ and the measured grain size was ~240 ± 100 nm after HPT through 200 turns [90].

A pronounced increase in the strain rate sensitivity is also observed in fine-grained pure magnesium tested at low strain rates and this effect is associated with an exceptional increase in ductility in this material [15, 23, 92]. It is important to note that experiments revealed a reduced activation energy of ~75 kJ/mol in this condition [15, 23]. Thus, the model predicts strain rate sensitivities of ~0.2 and larger for ultrafine-grained magnesium at low strain rates and this agrees with experimental observations. However, the predicted level of flow stress for magnesium is lower than the values observed experimentally and this is attributed to the presence of a threshold stress in this material. The significance of threshold stresses in these materials is discussed in the following section.

5. Significance of a threshold stress

The present model predicts that the flow stress is inversely proportional to the square root of the grain size during the low temperature deformation of coarse-grained materials and this is directly analogous to the well-established Hall-Petch relationship with the exception that this latter relationship also incorporates a threshold stress. Thus, the correlation between flow stress and grain size predicted for some pure metals agrees well with experimental data as shown in Fig. 2. However, experimental data shows that plots of σ as a function of $d^{-0.5}$ for iron [57] and titanium [93] follow trend lines that intersect the stress axis at a positive stress. This suggests that lattice friction may increase the stress required for deformation and this effect is then modeled by incorporating a threshold stress, σ_0. This means that eqs. (6) and (7) are re-written in the form

$$\dot{\varepsilon} \approx \frac{10\delta D_{gb}}{d^3}\left[exp\left(\frac{2d(\sigma-\sigma_0)^2 b^2}{3GkT}\right) - 1\right] \qquad (9)$$

and

$$\sigma \approx \sigma_0 + \sqrt{\frac{3GkT}{2db^2} ln\left(\frac{\dot{\varepsilon}d^3}{10\delta D_{gb}} + 1\right)} \quad (10)$$

Figure 9 shows the predicted variation of the flow stress as a function of the inverse of the square root of the grain size with the incorporation of a threshold stress for the three pure metals of (a) Fe, (b) Ti and (c) Al. Experimental data are also included in Fig. 9 for (a) Fe [52-57, 94, 95], (b) Ti (grades 1, 2 and 3 and Ti-6Al-4V) [96-114] and (c) Al (pure Al [35-41] and Al-Mg [115-117] alloys) where the threshold stress was based on the value reported for iron [94] and on a best fit to the data for Ti and Al. It is observed that the model predicts an almost linear relationship between σ and $d^{-0.5}$ but there is a small decrease in slope with decreasing grain size which is associated with the enhanced contribution of grain boundary sliding to the overall strain rate and the associated decrease in the climb distance.

The slopes of the curves in Fig. 9 display very good agreement with the experimental data for all materials and it is interesting to note that, although the model was derived specifically for grains smaller than the subgrain size, the slope predicted for coarse grains also agrees well with the experimental data. Thus, slopes of ~600 MPa $\mu m^{-0.5}$ and ~560 MPa $\mu m^{-0.5}$ are predicted for grains >1 μm in γ-Fe and α-Fe, respectively. A comparison of the experimental data for bulk iron (b.c.c., α-Fe) fabricated from powders and austenitic stainless steel (f.c.c., γ-Fe) indicates that the Hall-Petch coefficients in iron are essentially identical regardless of whether the crystal structure is b.c.c. or f.c.c. and with a slope of ~600 MPa $\mu m^{-0.5}$ [94]. The present model predicts almost identical behavior for both crystal structures and shows very good agreement with the slopes determined experimentally even though the input parameters of the Burgers vector modulus, the shear modulus and the grain boundary diffusion coefficient are different for the two crystal structures of γ-Fe and α-Fe.

It is important to note that the input for the model is based on the physical parameters of the pure metals and this does not include the effect of alloying elements. In practice, the presence of impurities can increase the stress required for dislocation glide and climb and this effect may also be modeled through the incorporation of a threshold stress. For example, the slope reported for the Ti-6% Al-4% V alloy agrees with the present model and the data fit a threshold stress of ~700 MPa which is higher than the stress observed in pure Ti. Furthermore, experimental data for pure aluminum and Al-Mg alloys both follow a Hall-Petch relationship with similar slopes but the Al-Mg alloys exhibit higher flow stresses [118]. Therefore, Fig. 9(c) also shows the relationship between σ and $d^{-0.5}$ predicted by the model for Al with (upper line) and without (lower line) a threshold stress. Again there is good agreement between the experimental data and the model and the experimental results for the coarser grains are also consistent with the model except for a slight disagreement at very small grain sizes in the Al-Mg alloys. All of the experimental data were obtained from samples processed by SPD and it is known that segregation of Mg occurs along the grain boundaries of Al at large total strains. Thus, the small increase in flow stress at these small grain sizes is probably associated with the presence of grain boundary segregation that has increased the threshold stress [119-122].

A recent report documented an inverse Hall-Petch behavior in a magnesium AZ91 alloy and in an AZ91-1% Al_2O_3 composite at grain sizes smaller than ~0.1 μm and this effect was attributed to an enhanced contribution from a diffusion-assisted creep mechanism [123]. However, the measured strain rate sensitivity was significantly lower than predicted either by Coble creep or by high temperature grain boundary sliding. Also, a change in slope in the Hall-Petch behavior was observed at grains smaller than ~1 μm and this effect is not directly explained by the advent of diffusion creep.

Nevertheless, despite this apparent dichotomy, all of these effects, including the change in slope at grains of ~1 μm, the inverse Hall-Petch behavior and the values of the strain rate sensitivity, are predicted by the present model for pure magnesium when considering a threshold stress of 200 MPa. Thus, Fig. 10(a) shows the predicted flow stress plotted as a function of the grain size at grain sizes smaller than a few microns using a threshold stress of 200 MPa, experimental data for the AZ91 alloy [123-132] and the empirical Hall-Petch prediction. It is readily apparent that the theoretical model predicts a slope which is smaller than observed in the empirical Hall-Petch curve and the high slope in the Hall-Petch curve is attributed to the occurrence of twinning in the coarser-grained magnesium. At grain sizes smaller than ~1 μm there is a change in slope in the experimental data and this demonstrates a good agreement with the present model thereby suggesting that the proposed deformation mechanism takes place in fine-grained magnesium.

In this connection it is important to note that the present deformation mechanism is expected to be rate-controlling only at grain sizes smaller than the equilibrium subgrain size. Therefore, the predicted subgrain size in Mg is also plotted in Fig. 10(a) as the dashed line lying at an angle to the experimental data and this prediction intersects the curve of flow stress at a grain size of ~0.3 μm. Thus, the change in slope observed in the experimental data correctly occurs when the grain size approaches the subgrain size and this supports the proposal that a different deformation mechanism then becomes operational. An inverse Hall-Petch behavior is predicted at grain sizes smaller than ~100 nm for a strain-rate of 10^{-4} s^{-1} and this also agrees with the experimental data.

Finally, it is important to note that the incorporation of a threshold stress into the theoretical model reduces the predicted strain rate sensitivity. In order to illustrate this effect, Fig. 10(b) shows the predicted flow stress for Mg with a grain size of 80 nm plotted as a function of the strain rate without a threshold stress (lower dashed line) and when a threshold stress of 200 MPa is incorporated in the model (upper solid line) and it is clear that the slope is reduced in the latter plot. In practice, experimental data reported for an AZ91-1% Al_2O_3 composite processed by HPT with a grain size of ~80 nm [123] is also plotted and these results show very good agreement with the prediction when the threshold stress is included.

6. High temperature behavior

Increasing the testing temperature reduces the flow stress of metallic materials and this agrees with the prediction from the present model. Furthermore, the model predicts a decrease in the slope of the Hall-Petch plots and an increase in the strain rate sensitivity with increasing temperature and these predictions are in agreement with experimental observations. For example, Fig. 11 shows experimental data for the yield stress of type 316L austenitic stainless steel at three different temperatures plotted as a function of the inverse of the grain size where the spatial grain size was determined as $d = 1.7 \times \bar{L}$, where $\bar{L}$ is the mean linear intercept length [95]. It is apparent that the slope decreases at higher temperatures and the predictions from the model, as shown by the solid lines, are in good agreement with the experimental data. It is worth noting also that the threshold stress decreases at high temperatures but is essentially the same at 673 and 873 K.

The trend of a decrease in the H-P slope with an increase in temperature was also reported in magnesium [133] and the predicted slope agrees with experimental data at temperatures higher than ~373 K. Magnesium and magnesium alloys exhibit significant twinning in samples with coarse grain sizes and when testing at low temperatures this twinning is associated with a higher H-P slope [134]. However, as the grain size decreases and/or the temperature increases, the deformation becomes slip-controlled and the experimental data then agree with the present model. For example, it was shown that the predicted slope agrees with experimental data for a magnesium AZ91 alloy with fine grain sizes at room temperature as illustrated in Fig. 10. Figure 12 shows experimental data of the flow stress for a magnesium AZ31 alloy at different temperatures plotted as a function of the inverse of the square root of the grain size with the grain size again determined as $d = 1.7 \times \overline{L}$ [134]. It is seen that the model agrees with the data for high temperature deformation and the same result is observed for a similar alloy tested in tension at different temperatures [135].

In addition to the decrease in flow stress and in the H-P slope with increasing temperature, an increase in strain rate sensitivity is also generally observed. In fact, a strain rate sensitivity of ~0.5, which is associated with superplasticity [88, 136], may be observed in specific strain rate ranges in fine-grained metallic materials at high temperatures. The present model specifically predicts this trend since it incorporates the model for superplastic deformation [19].

It has been shown that the model for superplasticity, in which the rate-controlling mechanism is grain boundary sliding, agrees with experimental data [137-141] and there are several comprehensive summaries of the data [142-144]. Accordingly, Fig. 13(a) shows the flow stress observed in a fine-grained aluminum alloy tested at different temperatures and plotted as a function of strain rate [118] together with the predictions from the model shown as solid lines. The predicted strain rate sensitivity, *m*, is also plotted as a function of strain rate in Fig. 13(b). The agreement between the experimental data and the model is excellent in the plot of flow stress versus strain rate and both the experimental results and the model display a continuous curve with reduced slope at room temperature and a sigmoidal-shaped curve for the strain rate sensitivity and three distinct regions at high temperatures.

A sigmoidal shape of the type shown in Fig. 13(b) is consistent with experimental data in superplastic metals [145, 146] and it may be explained as follows. The deformation rate is controlled by the rate of diffusion of defects created by dislocation climb at the head of the pile-up. As the strain rate decreases, the rate of defect generation also decreases and moves toward the condition of thermal equilibrium. In this condition, the approximation described in eq. 3 becomes valid and the strain rate sensitivity tends to 0.5 [19]. Therefore, an increase in the strain rate sensitivity is expected with decreasing strain rate and similarly there is a decrease in *m* at high strain rates. The decrease in *m* at very low stresses is associated with the presence of threshold stress and a simple procedure is now available for estimating and interpreting the magnitude of the threshold stress under high temperature creep conditions [147, 148]. Experiments have shown that this threshold stress is associated with the presence of impurity atoms in the grain boundaries which, following Fig. 1, impede the climb of extrinsic dislocations into and along the opposite boundaries. This interpretation is confirmed by direct experimental evidence showing that the region of high strain rate sensitivity at intermediate stresses may be extended to very low stresses in materials of exceptionally high purity, thereby negating the region of low *m* which is generally observed at the lowest experimental strain rates [149, 150].

In practice, it is now established that grain boundary sliding is the rate-controlling mechanism associated with superplasticity [151] and this is related to a strain rate sensitivity of ~0.5 and elongations in tension of over ~400% [88, 136]. By contrast, when the rate-controlling flow process is viscous glide at high temperatures, as when dislocations drag solute atmospheres during glide in solid solution alloys, the strain rate sensitivity is $m \approx 0.33$ and there is enhanced ductility but with total elongations that may be up to but only slightly larger than 300% [152, 153]. This latter behavior is not an example of true superplasticity and instead it represents the principle of the so-called Quick Plastic Forming (QPF) technology which is employed as a hot blow-forming process in the production of aluminum panels for use in automotive applications [154].

In practice, the fabrication of ultrafine-grained metals using SPD processing presents new opportunities for making use of superplastic forming in industrial applications [155] and these opportunities are based primarily on the occurrence of superplastic flow at higher strain rates when the grain size is reduced [156, 157]. For example, industrial superplastic forming is generally conducted at strain rates of ~10^{-3} – 10^{-2} s^{-1} which requires a typical forming time for sheet metals of ~20 – 30 minutes [158] whereas the ultrafine grains produced by SPD processing give excellent superplastic behavior at strain rates of ~10^{-2} – 1 s^{-1} and this provides the potential for using forming time of <60 seconds.

High elongations of >300% associated with moderate strain rate sensitivities of ~0.2 ~ 0.3 have been reported in magnesium alloys processed by SPD and tested at moderate temperatures [159-163]. As already noted, the traditional grain boundary sliding mechanism [19] predicts a gradual decrease in strain rate sensitivity with increasing strain rate and/or due to the presence of a significant threshold stress. Figure 14 shows the prediction of flow stress and strain rate sensitivity as a function of strain rate for the fine-grained magnesium AZ31 alloy at 423 K together with experimental values of the flow stress determined for the alloy [160, 162]. A grain size of 1 μm was estimated for the AZ31 alloy processed by HPT and heated to 423 K [164]. Thus, a sigmoidal-shaped curve is predicted by the model and this is associated with a peak strain rate sensitivity of $m \approx 0.2$ at ~10^{-4} s^{-1}. This means that, although the condition for superplasticity of $m \approx 0.5$ is not met under these conditions, a reasonably high strain rate sensitivity develops in this fine-grained magnesium alloy and this is associated with good ductilities at this testing temperature.

7. Comparison between experimental data and the model for a wide range of metals

It is shown in this report that the model proposed for flow behavior agrees well with experimental data for several different metals and alloys. However, in order to more fully clarify the validity of the model, it is important to establish a detailed comparison between the measured experimental flow stresses and the flow stresses predicted by the model.

Figure 15 shows the values of the flow stress determined experimentally and then plotted as a function of the flow stress predicted by the present model. This plot contains data from a very wide range of different metals and alloys with over three orders of magnitude of grain sizes and strain rates and various testing temperatures. The input parameters for the model are summarized in detail in Table 2 with the appropriate references which are given here: Al [29, 35-41, 115, 116, 118], Cu [18, 22, 42-51, 165], Fe (α) [52-58, 166], Fe (α+γ) [167], Fe (γ) [94, 95], Mg [23, 123, 133-135, 137, 140, 141, 159, 160, 162, 168], Ni [14, 59-62], Ti [96-114, 169] and Zn [86, 91, 170-172]. A strain rate of 10^{-4} s^{-1} was taken when using experimental results from microhardness investigations.

In constructing Fig. 15, it is important to emphasize that the various experimental results may be subjected to significant inaccuracies. Thus, there are many reports documenting a broad distribution of grain sizes, such as in gradient materials [173], and grain shapes which often makes it difficult to determine a value for a critical estimate of the deformation behavior. Also, it is known that the value of the grain size is dependent upon the method used in the measurement. Therefore, the results are plotted using the reported value for the grain size unless there was a clear specification of measuring the mean linear intercept grain size, $\bar{L}$. For the latter examples, the spatial grain size was then estimated as $d = 1.7 \times \bar{L}$. The yield stress is also subject to inaccuracy since the transition from elastic to plastic behavior is not always clearly defined in many experimental situations, especially when extensometers are not used and the tests are conducted on miniature specimens and/or at high temperatures.

Notwithstanding the difficulties associated with scatter in the experimental data, an examination of Fig. 15 shows that the agreement between the experiments and the theoretical model is remarkably good with all datum points, for eight different materials, lying on or about the prediction from the model. This is a significant result because the input parameters used in the analyses are not adjustable except only for the possible presence of a threshold stress in some of the experiments. However, even the values of the threshold stresses are generally in agreement with the experimental observations. Also, there is a decrease in threshold stress with increasing temperature and decreasing strain rate and this leads to a very minor contribution from the threshold stress at the higher temperatures and in low strain rate deformation. One parameter also affecting the effectiveness of the present model is the presence and occurrence of twins. It was noted earlier that the present model does not agree well with experimental data for magnesium under conditions where twinning is significant but nevertheless the model agrees well with data for fine-grained magnesium and at high temperatures where twinning is absent.

It is important to note also the experimental observation of higher experimental flow stresses than predicted in Al-Mg alloys processed by HPT [115, 117]. It is now known that a segregation of impurity atoms may take place along grain boundaries after severe plastic deformation [174-178] and this effect is readily observed in Al-Mg alloys [119, 179, 180]. Thus, the apparent disagreement between experimental data and the model in this case provides supporting evidence in favor of the present model. The reason is because the segregation increases the concentration of Mg atoms along the Al grain boundaries and this will increase the resistance to grain boundary sliding in these areas and thereby increase the threshold stress. This means in practice that the value used as a threshold stress for the solid solution alloy should increase in the presence of impurity segregation along the grain boundaries.

8. Summary and conclusions

- A comprehensive model for the deformation behavior of metals is proposed based on grain boundary sliding through dislocation glide. The rate of dislocation climb at the head of a pile-up is considered as the rate-controlling mechanism where this is analogous to the conventional deformation mechanism for high temperature grain boundary sliding [19] which is associated with superplasticity.
- The model predicts a steady-state deformation for fine-grained materials in which the grain size is smaller than the stable sub-grain size and there is no strain hardening. Nevertheless, the model also predicts well the yield stress of coarse-grained metals when no substructure is present.
- The model is capable of predicting the flow stress, strain rate and strain rate sensitivity for pure metals using basic metal properties such as the shear modulus, the Burgers vector modulus and the grain boundary diffusion coefficient. The incorporation of a threshold stress improves the agreement with experimental data for some metals and alloys.
- There is a very good agreement between the present model and published experimental data for a range of different metals including aluminum, copper, iron (b.c.c. and f.c.c.), magnesium, nickel, titanium and zinc and some alloys covering over 3 orders of magnitude of grain sizes and with the experiments conducted at different strain rates and temperatures.
- There is a good agreement between the predicted slope, at different temperatures, in the relationship between the flow stress and the grain size for a broad range of grain

sizes. This result shows that the mechanism provides an estimation of the Hall-Petch slope for different materials.

- The model predicts several experimentally-observed effects such as a stable grain size after HPT processing, an inverse Hall-Petch behavior and an increase in the strain rate sensitivity in different metals.

Acknowledgements

One of the authors was supported by CNPq under Grant Agreements 302445/2018-8 and 400407/2016-7 and by the Serrapilheira Institute under Grant Agreement Serra-1709-17750 (RBF). The other author was supported by the European Research Council under ERC Grant Agreement No. 267464-SPDMETALS (TGL).

References

[1] Kocks UF, Mecking H. Physics and phenomenology of strain hardening: the FCC case. Progress in Materials Science. 2003;48:171-273.
[2] Zehetbauer M, Seumer V. Cold work hardening in stages IV and V of F.C.C. metals—I. Experiments and interpretation. Acta Metallurgica et Materialia. 1993;41:577-88.
[3] Zhu YT, Lowe TC, Langdon TG. Performance and applications of nanostructured materials produced by severe plastic deformation. Scripta Materialia. 2004;51:825-30.
[4] Valiev RZ, Estrin Y, Horita Z, Langdon TG, Zehetbauer MJ, Zhu YT. Producing bulk ultrafine-grained materials by severe plastic deformation. JOM. 2006;58 (4):33-9.
[5] Mohamed FA, Yang H. Deformation Mechanisms in Nanocrystalline Materials. Metallurgical and Materials Transactions A. 2010;41:823-37.
[6] Valiev RZ, Islamgaliev RK, Alexandrov IV. Bulk nanostructured materials from severe plastic deformation. Progress in Materials Science. 2000;45:103-87.
[7] Hall EO. The deformation and ageing of mild steel 3. Discussion of results. Proceedings of the Physical Society of London Section B. 1951;64:747-53.
[8] Petch NJ. The cleavage strength of polycrystals. Journal of the Iron and Steel Institute. 1953;174:25-8.
[9] Chokshi AH, Rosen A, Karch J, Gleiter H. On the validity of the hall-petch relationship in nanocrystalline materials. Scripta Metallurgica. 1989;23:1679-83.
[10] Nieh TG, Wadsworth J. Hall-Petch relation in nanocrystalline solids. Scripta Metallurgica et Materialia. 1991;25:955-8.
[11] Iwahashi Y, Horita Z, Nemoto M, Langdon TG. Factors influencing the equilibrium grain size in equal-channel angular pressing: Role of Mg additions to aluminum. Metallurgical and Materials Transactions A. 1998;29:2503-10.
[12] Goloborodko A, Sitdikov O, Kaibyshev R, Miura H, Sakai T. Effect of pressing temperature on fine-grained structure formation in 7475 aluminum alloy during ECAP. Materials Science and Engineering: A. 2004;381:121-8.

[13] Conrad H. Grain size dependence of the plastic deformation kinetics in Cu. Materials Science and Engineering: A. 2003;341:216-28.
[14] Krasilnikov N, Lojkowski W, Pakiela Z, Valiev R. Tensile strength and ductility of ultra-fine-grained nickel processed by severe plastic deformation. Materials Science and Engineering: A. 2005;397:330-7.
[15] Somekawa H, Mukai T. Hall–Petch breakdown in fine-grained pure magnesium at low strain rates. Metallurgical and Materials Transactions A. 2015;46:894-902.
[16] Mohamed FA, Dheda SS. On the minimum grain size obtainable by high-pressure torsion. Materials Science and Engineering: A. 2012;558:59-63.
[17] Mohamed FA, Dheda SS. On the minimum grain size obtainable by equal channel angular pressing. Materials Science and Engineering: A. 2013;580:227-30.
[18] Edalati K, Horita Z. High-pressure torsion of pure metals: Influence of atomic bond parameters and stacking fault energy on grain size and correlation with hardness. Acta Materialia. 2011;59:6831-6.
[19] Langdon TG. A unified approach to grain boundary sliding in creep and superplasticity. Acta Metallurgica et Materialia. 1994;42:2437-43.
[20] Setman D, Schafler E, Korznikova E, Zehetbauer MJ. The presence and nature of vacancy type defects in nanometals detained by severe plastic deformation. Materials Science and Engineering: A. 2008;493:116-22.
[21] Chinh NQ, Szommer P, Horita Z, Langdon TG. Experimental evidence for grain-boundary sliding in ultrafine-grained aluminum processed by severe plastic deformation. Advanced Materials. 2006;18:34-9.
[22] Valiev RZ, Kozlov EV, Ivanov YF, Lian J, Nazarov AA, Baudelet B. Deformation behaviour of ultra-fine-grained copper. Acta Metallurgica et Materialia. 1994;42:2467-75.
[23] Figueiredo RB, Sabbaghianrad S, Giwa A, Greer JR, Langdon TG. Evidence for exceptional low temperature ductility in polycrystalline magnesium processed by severe plastic deformation. Acta Materialia. 2017;122:322-31.
[24] Mohamed FA. On the creep transition from superplastic behavior to nanocrystalline behavior. Materials Science and Engineering: A. 2016;655:396-8.
[25] Langdon TG. Twenty-five years of ultrafine-grained materials: Achieving exceptional properties through grain refinement. Acta Materialia. 2013;61:7035-59.
[26] Valiev RZ, Langdon TG. Principles of equal-channel angular pressing as a processing tool for grain refinement. Progress in Materials Science. 2006;51:881-981.
[27] Zhilyaev AP, Langdon TG. Using high-pressure torsion for metal processing: Fundamentals and applications Progress in Materials Science. 2008;53:893-979.
[28] Friedel J. Dislocations. Oxford, U.K.: Pergamon Press; 1964. p. 104-33.
[29] Chinh NQ, Csanádi T, Győri T, Valiev RZ, Straumal BB, Kawasaki M, et al. Strain rate sensitivity studies in an ultrafine-grained Al–30wt.% Zn alloy using micro- and nanoindentation. Materials Science and Engineering: A. 2012;543:117-20.
[30] J.E. Bird, A.K. Mukherjee, Dorn JE. Quantitative Relation Between Properties and Microstructure. Jerusalem, Israel: Israel Universities Press; 1969.
[31] Cannon WR, Langdon TG. Creep of ceramics. Journal of Materials Science. 1988;23:1-20.
[32] Twiss RJ. Theory and applicability of a recrystallized grain size paleopiezometer. Pure and Applied Geophysics. 1977;115:227-44.
[33] White S. Grain and sub-grain size variations across a mylonite zone. Contributions to Mineralogy and Petrology. 1979;70:193-202.
[34] Frost; HJ, Ashby MF. Deformation-Mechanism Maps: The Plasticity and Creep of Metals and Ceramics. Oxford, U.K.: Pergamon Press; 1982.

[35] Tsuji N, Okuno S, Matsuura T, Koizumi Y, Minamino Y. Mechanical properties as a function of grain size in ultrafine grained aluminum and iron fabricated by ARB and annealing process. Materials Science Forum. 2003;426-432:2667-72.
[36] Edalati K, Cubero-Sesin JM, Alhamidi A, Mohamed IF, Horita Z. Influence of severe plastic deformation at cryogenic temperature on grain refinement and softening of pure metals: Investigation using high-pressure torsion. Materials Science and Engineering: A. 2014;613:103-10.
[37] Horita Z, Fujinami T, Nemoto M, Langdon TG. Equal-channel angular pressing of commercial aluminum alloys: Grain refinement, thermal stability and tensile properties. Metallurgical and Materials Transactions A. 2000;31:691-701.
[38] Bachmaier A, Pippan R. Effect of oxide particles on the stabilization and final microstructure in aluminium. Materials Science and Engineering: A. 2011;528:7589-95.
[39] Chen X, Huang G-S, Liu S-S, Han T-Z, Jiang B, Tang A-T, et al. Grain refinement and mechanical properties of pure aluminum processed by accumulative extrusion bonding. Transactions of Nonferrous Metals Society of China. 2019;29:437-47.
[40] Hayes RW, Witkin D, Zhou F, Lavernia EJ. Deformation and activation volumes of cryomilled ultrafine-grained aluminum. Acta Materialia. 2004;52:4259-71.
[41] Huang Y, Bazarnik P, Wan D, Luo D, Pereira PHR, Lewandowska M, et al. The fabrication of graphene-reinforced Al-based nanocomposites using high-pressure torsion. Acta Materialia. 2019;164:499-511.
[42] Jenei P, Yoon EY, Gubicza J, Kim HS, Lábár JL, Ungár T. Microstructure and hardness of copper–carbon nanotube composites consolidated by High Pressure Torsion. Materials Science and Engineering: A. 2011;528:4690-5.
[43] Gubicza J, Dobatkin SV, Khosravi E, Kuznetsov AA, Lábár JL. Microstructural stability of Cu processed by different routes of severe plastic deformation. Materials Science and Engineering: A. 2011;528:1828-32.
[44] Zhilyaev AP, Swaminathan S, Gimazov AA, McNelley TR, Langdon TG. An evaluation of microstructure and microhardness in copper subjected to ultra-high strains. Journal of Materials Science. 2008;43:7451-6.
[45] Almazrouee AI, Al-Fadhalah KJ, Alhajeri SN, Langdon TG. Microstructure and microhardness of OFHC copper processed by high-pressure torsion. Materials Science and Engineering: A. 2015;641:21-8.
[46] Wang YM, Ma E. Three strategies to achieve uniform tensile deformation in a nanostructured metal. Acta Materialia. 2004;52:1699-709.
[47] Horita Z, Langdon TG. Microstructures and microhardness of an aluminum alloy and pure copper after processing by high-pressure torsion. Materials Science and Engineering: A. 2005;410-411:422-5.
[48] An XH, Wu SD, Zhang ZF, Figueiredo RB, Gao N, Langdon TG. Evolution of microstructural homogeneity in copper processed by high-pressure torsion. Scripta Materialia. 2010;63:560-3.
[49] Flinn JE, Field DP, Korth GE, Lillo TM, Macheret J. The flow stress behavior of OFHC polycrystalline copper. Acta Materialia. 2001;49:2065-74.
[50] Tian YZ, Gao S, Zhao LJ, Lu S, Pippan R, Zhang ZF, et al. Remarkable transitions of yield behavior and Lüders deformation in pure Cu by changing grain sizes. Scripta Materialia. 2018;142:88-91.
[51] Schafler E, Kerber MB. Microstructural investigation of the annealing behaviour of high-pressure torsion (HPT) deformed copper. Materials Science and Engineering: A. 2007;462:139-43.

[52] Edalati K, Fujioka T, Horita Z. Evolution of Mechanical Properties and Microstructures with Equivalent Strain in Pure Fe Processed by High Pressure Torsion. Materials Transactions. 2009;50:44-50.
[53] Wetscher F, Vorhauer A, Stock R, Pippan R. Structural refinement of low alloyed steels during severe plastic deformation. Materials Science and Engineering: A. 2004;387-389:809-16.
[54] Valiev RZ, Ivanisenko YV, Rauch EF, Baudelet B. Structure and deformaton behaviour of Armco iron subjected to severe plastic deformation. Acta Materialia. 1996;44:4705-12.
[55] Hohenwarter A, Kammerhofer C, Pippan R. The ductile to brittle transition of ultrafine-grained Armco iron: an experimental study. Journal of Materials Science. 2010;45:4805-12.
[56] Muñoz JA, Higuera OF, Benito JA, Bradai D, Khelfa T, Bolmaro RE, et al. Analysis of the micro and substructural evolution during severe plastic deformation of ARMCO iron and consequences in mechanical properties. Materials Science and Engineering: A. 2019;740-741:108-20.
[57] Tejedor R, Edalati K, Benito JA, Horita Z, Cabrera JM. High-pressure torsion of iron with various purity levels and validation of Hall-Petch strengthening mechanism. Materials Science and Engineering: A. 2019;743:597-605.
[58] Borchers C, Garve C, Tiegel M, Deutges M, Herz A, Edalati K, et al. Nanocrystalline steel obtained by mechanical alloying of iron and graphite subsequently compacted by high-pressure torsion. Acta Materialia. 2015;97:207-15.
[59] Zhang HW, Huang X, Pippan R, Hansen N. Thermal behavior of Ni (99.967% and 99.5% purity) deformed to an ultra-high strain by high pressure torsion. Acta Materialia. 2010;58:1698-707.
[60] Bachmaier A, Hohenwarter A, Pippan R. New procedure to generate stable nanocrystallites by severe plastic deformation. Scripta Materialia. 2009;61:1016-9.
[61] Dalla Torre F, Spätig P, Schäublin R, Victoria M. Deformation behaviour and microstructure of nanocrystalline electrodeposited and high pressure torsioned nickel. Acta Materialia. 2005;53:2337-49.
[62] Hughes GD, Smith SD, Pande CS, Johnson HR, Armstrong RW. Hall-petch strengthening for the microhardness of twelve nanometer grain diameter electrodeposited nickel. Scripta Metallurgica. 1986;20:93-7.
[63] Tabor D. The Hardness of Metals. Oxford, U.K.: Clarendon Press; 1951.
[64] Edalati K, Yamamoto A, Horita Z, Ishihara T. High-pressure torsion of pure magnesium: Evolution of mechanical properties, microstructures and hydrogen storage capacity with equivalent strain. Scripta Materialia. 2011;64:880-3.
[65] Naghdy S, Kestens L, Hertelé S, Verleysen P. Evolution of microstructure and texture in commercial pure aluminum subjected to high pressure torsion processing. Materials Characterization. 2016;120:285-94.
[66] Hebesberger T, Stüwe HP, Vorhauer A, Wetscher F, Pippan R. Structure of Cu deformed by high pressure torsion. Acta Materialia. 2005;53:393-402.
[67] Mohamed FA, Langdon TG. Creep at low stress levels in the superplastic Zn-22% Al eutectoid. Acta Metallurgica. 1975;23:117-24.
[68] Cao Y, Kawasaki M, Wang YB, Alhajeri SN, Liao XZ, Zheng WL, et al. Unusual macroscopic shearing patterns observed in metals processed by high-pressure torsion. Journal of Materials Science. 2010;45:4545-53.
[69] Cao Y, Wang YB, Alhajeri SN, Liao XZ, Zheng WL, Ringer SP, et al. A visualization of shear strain in processing by high-pressure torsion. Journal of Materials Science. 2010;45:765-70.

[70] Cao Y, Wang YB, Figueiredo RB, Chang L, Liao XZ, Kawasaki M, et al. Three-dimensional shear-strain patterns induced by high-pressure torsion and their impact on hardness evolution. Acta Materialia. 2011;59:3903-14.
[71] Kulagin R, Beygelzimer Y, Ivanisenko Y, Mazilkin A, Straumal B, Hahn H. Instabilities of interfaces between dissimilar metals induced by high pressure torsion. Materials Letters. 2018;222:172-5.
[72] Kulagin R, Beygelzimer Y, Bachmaier A, Pippan R, Estrin Y. Benefits of pattern formation by severe plastic deformation. Applied Materials Today. 2019;15:236-41.
[73] Estrin Y, Beygelzimer Y, Kulagin R. Design of architectured materials based on mechanically driven structural and compositional patterning. Advanced Engineering Materials. 2019;21:1900487.
[74] Jiang W, Zhou H, Cao Y, Nie J, Li Y, Zhao Y, et al. On the heterogeneity of local shear strain induced by high-pressure torsion. Advanced Engineering Materials. 2020;22:1900477.
[75] Huang Y, Kawasaki M, Langdon TG. Influence of anvil alignment on shearing patterns in high-pressure torsion. Advanced Engineering Materials. 2013;15:747-55.
[76] Huang Y, Kawasaki M, Langdon TG. An investigation of flow patterns and hardness distributions using different anvil alignments in high-pressure torsion. Journal of Materials Science. 2013;48:4533-42.
[77] Huang Y, Kawasaki M, Langdon TG. An evaluation of the shearing patterns introduced by different anvil alignments in high-pressure torsion. Journal of Materials Science. 2014;49:3146-57.
[78] Huang Y, Kawasaki M, Al-Zubaydi A, Langdon TG. Effect of anvil roughness on the flow patterns and hardness development in high-pressure torsion. Journal of Materials Science. 2014;49:6517-28.
[79] Divinski SV, Reglitz G, Rösner H, Estrin Y, Wilde G. Ultra-fast diffusion channels in pure Ni severely deformed by equal-channel angular pressing. Acta Materialia. 2011;59:1974-85.
[80] Li J, Xu W, Wu X, Ding H, Xia K. Effects of grain size on compressive behaviour in ultrafine grained pure Mg processed by equal channel angular pressing at room temperature. Materials Science and Engineering: A. 2011;528:5993-8.
[81] Valiev RZ, Gertsman VY, Kaibyshev OA. Non-equilibrium state and recovery of grain boundary structure. II. Energetic analysis. Physica Status Solidi a-Applied Research. 1983;78:177-86.
[82] Nazarov AA, Romanov AE, Valiev RZ. On the structure, stress fields and energy of nonequilibrium grain boundaries. Acta Metallurgica et Materialia. 1993;41:1033-40.
[83] Horita Z, Smith DJ, Furukawa M, Nemoto M, Valiev RZ, Langdon TG. An investigation of grain boundaries in submicrometer-grained Al-Mg solid solution alloys using high-resolution electron microscopy. Journal of Materials Research. 1996;11:1880-90.
[84] Figueiredo RB, Poggiali FSJ, Silva CLP, Cetlin PR, Langdon TG. The influence of grain size and strain rate on the mechanical behavior of pure magnesium. Journal of Materials Science. 2016;51:3013-24.
[85] Edalati K, Horita Z. Significance of homologous temperature in softening behavior and grain size of pure metals processed by high-pressure torsion. Materials Science and Engineering: A. 2011;528:7514-23.
[86] Kawasaki M, Ahn B, Langdon TG. Microstructural evolution in a two-phase alloy processed by high-pressure torsion. Acta Materialia. 2010;58:919-30.

[87] Valiev RZ, Alexandrov IV, Zhu YT, Lowe TC. Paradox of strength and ductility in metals processed by severe plastic deformation. Journal of Materials Research. 2011;17:5-8.
[88] Kawasaki M, Figueiredo RB, Langdon TG. The requirements for superplasticity with an emphasis on magnesium alloys. Advanced Engineering Materials. 2016;18:127-31.
[89] Edalati K, Horita Z, Valiev RZ. Transition from poor ductility to room-temperature superplasticity in a nanostructured aluminum alloy. Scientific Reports. 2018;8:6740.
[90] Edalati K, Masuda T, Arita M, Furui M, Sauvage X, Horita Z, et al. Room-temperature superplasticity in an ultrafine-grained magnesium alloy. Scientific Reports. 2017;7.
[91] Kawasaki M, Lee H-J, Choi I-C, Jang J-i, Ahn B, Langdon TG. Evolution of hardness, microstructure, and strain rate sensitivity in a Zn-22% Al eutectoid alloy processed by high-pressure torsion. IOP Conference Series: Materials Science and Engineering. 2014;63:012101.
[92] Zeng Z, Nie J-F, Xu S-W, H. J. Davies C, Birbilis N. Super-formable pure magnesium at room temperature. Nature Communications. 2017;8:972.
[93] Wang CT, Gao N, Gee MG, Wood RJK, Langdon TG. Tribology testing of ultrafine-grained Ti processed by high-pressure torsion with subsequent coating. Journal of Materials Science. 2013;48:4742-8.
[94] Takaki S, Kawasaki K, Kimura Y. Mechanical properties of ultra fine grained steels. Journal of Materials Processing Technology. 2001;117:359-63.
[95] Kashyap BP, Tangri K. On the Hall-Petch relationship and substructural evolution in type 316L stainless steel. Acta Metallurgica et Materialia. 1995;43:3971-81.
[96] Wang CT, Gao N, Gee MG, Wood RJK, Langdon TG. Effect of grain size on the micro-tribological behavior of pure titanium processed by high-pressure torsion. Wear. 2012;280-281:28-35.
[97] Zhao X, Fu W, Yang X, Langdon TG. Microstructure and properties of pure titanium processed by equal-channel angular pressing at room temperature. Scripta Materialia. 2008;59:542-5.
[98] Zhao X, Yang X, Liu X, Wang X, Langdon TG. The processing of pure titanium through multiple passes of ECAP at room temperature. Materials Science and Engineering: A. 2010;527:6335-9.
[99] Ko YG, Shin DH, Park K-T, Lee CS. An analysis of the strain hardening behavior of ultra-fine grain pure titanium. Scripta Materialia. 2006;54:1785-9.
[100] Yapici GG, Karaman I, Maier HJ. Mechanical flow anisotropy in severely deformed pure titanium. Materials Science and Engineering: A. 2006;434:294-302.
[101] Stolyarov VV, Zeipper L, Mingler B, Zehetbauer M. Influence of post-deformation on CP-Ti processed by equal channel angular pressing. Materials Science and Engineering: A. 2008;476:98-105.
[102] Kang D-H, Kim T-W. Mechanical behavior and microstructural evolution of commercially pure titanium in enhanced multi-pass equal channel angular pressing and cold extrusion. Materials & Design. 2010;31:S54-S60.
[103] Purcek G, Yapici GG, Karaman I, Maier HJ. Effect of commercial purity levels on the mechanical properties of ultrafine-grained titanium. Materials Science and Engineering: A. 2011;528:2303-8.
[104] Zhang Y, Figueiredo RB, Alhajeri SN, Wang JT, Gao N, Langdon TG. Structure and mechanical properties of commercial purity titanium processed by ECAP at room temperature. Materials Science and Engineering A. 2011;528:7708-14.

[105] Sordi VL, Ferrante M, Kawasaki M, Langdon TG. Microstructure and tensile strength of grade 2 titanium processed by equal-channel angular pressing and by rolling. Journal of Materials Science. 2012;47:7870-6.
[106] Stolyarov VV, Zhu YT, Lowe TC, Islamgaliev RK, Valiev RZ. A two step SPD processing of ultrafine-grained titanium. Nanostructured Materials. 1999;11:947-54.
[107] Sergueeva AV, Stolyarov VV, Valiev RZ, Mukherjee AK. Advanced mechanical properties of pure titanium with ultrafine grained structure. Scripta Materialia. 2001;45:747-52.
[108] Stolyarov VV, Zhu YT, Alexandrov IV, Lowe TC, Valiev RZ. Influence of ECAP routes on the microstructure and properties of pure Ti. Materials Science and Engineering: A. 2001;299:59-67.
[109] Stolyarov VV, Zhu YT, Lowe TC, Valiev RZ. Microstructure and properties of pure Ti processed by ECAP and cold extrusion. Materials Science and Engineering: A. 2001;303:82-9.
[110] Stolyarov VV, Zhu YT, Alexandrov IV, Lowe TC, Valiev RZ. Grain refinement and properties of pure Ti processed by warm ECAP and cold rolling. Materials Science and Engineering: A. 2003;343:43-50.
[111] Sabirov I, Valiev RZ, Semenova IP, Pippan R. Effect of equal channel angular pressing on the fracture behavior of commercially pure titanium. Metallurgical and Materials Transactions A. 2010;41:727-33.
[112] Figueiredo RB, de C. Barbosa ER, Zhao X, Yang X, Liu X, Cetlin PR, et al. Improving the fatigue behavior of dental implants through processing commercial purity titanium by equal-channel angular pressing. Materials Science and Engineering A. 2014;619:312-8.
[113] Salishchev GA, Galeyev RM, Malysheva SP, Myshlyaev MM. Structure and density of submicrocrystalline titanium produced by severe plastic deformation. Nanostructured Materials. 1999;11:407-14.
[114] Luo P, McDonald DT, Xu W, Palanisamy S, Dargusch MS, Xia K. A modified Hall–Petch relationship in ultrafine-grained titanium recycled from chips by equal channel angular pressing. Scripta Materialia. 2012;66:785-8.
[115] Furukawa M, Horita Z, Nemoto M, Valiev RZ, Langdon TG. Microhardness measurements and the Hall-Petch relationship in an Al-Mg alloy with submicrometer grain size. Acta Materialia. 1996;44:4619-29.
[116] Hayes JS, Keyte R, Prangnell PB. Effect of grain size on tensile behaviour of a submicron grained Al–3 wt-%Mg alloy produced by severe deformation. Materials Science and Technology. 2000;16:1259-63.
[117] Valiev RZ, Chmelik F, Bordeaux F, Kapelski G, Baudelet B. The Hall-Petch relation in submicro-grained Al-1.5% Mg alloy. Scripta Metallurgica et Materialia. 1992;27:855-60.
[118] Pereira PHR, Wang YC, Huang Y, Langdon TG. Influence of grain size on the flow properties of an Al-Mg-Sc alloy over seven orders of magnitude of strain rate. Materials Science and Engineering: A. 2017;685:367-76.
[119] Valiev RZ, Enikeev NA, Murashkin MY, Kazykhanov VU, Sauvage X. On the origin of the extremely high strength of ultrafine-grained Al alloys produced by severe plastic deformation. Scripta Materialia. 2010;63:949-52.
[120] Sauvage X, Wilde G, Divinski SV, Horita Z, Valiev RZ. Grain boundaries in ultrafine grained materials processed by severe plastic deformation and related phenomena. Materials Science and Engineering: A. 2012;540:1-12.

[121] Valiev RZ, Estrin Y, Horita Z, Langdon TG, Zehetbauer MJ, Zhu YT. Fundamentals of Superior Properties in Bulk NanoSPD Materials. Materials Research Letters. 2016;4:1-21.
[122] Balasubramanian N, Langdon TG. The strength–grain size relationship in ultrafine-grained metals. Metallurgical and Materials Transactions A. 2016;47:5827-38.
[123] Castro MM, Pereira PHR, Isaac A, Langdon TG, Figueiredo RB. Inverse Hall–Petch behaviour in an AZ91 alloy and in an AZ91–Al2O3 composite consolidated by high-pressure torsion. Advanced Engineering Materials. 2019;n/a:1900894.
[124] Khani S, Aboutalebi MR, Salehi MT, Samim HR, Palkowski H. Microstructural development during equal channel angular pressing of as-cast AZ91 alloy. Materials Science and Engineering: A. 2016;678:44-56.
[125] Chino Y, Mabuchi M. Influences of grain size on mechanical properties of extruded AZ91 Mg alloy after different extrusion processes. Advanced Engineering Materials. 2001;3:981-3.
[126] Chen B, Lin D-L, Jin L, Zeng X-Q, Lu C. Equal-channel angular pressing of magnesium alloy AZ91 and its effects on microstructure and mechanical properties. Materials Science and Engineering: A. 2008;483-484:113-6.
[127] Chung CW, Ding RG, Chiu YL, Hodgson MA, Gao W. Microstructure and mechanical properties of an as-cast AZ91 magnesium alloy processed by equal channel angular pressing. IOP Conference Series: Materials Science and Engineering. 2009;4:012012.
[128] Kim WJ, Jeong HG, Jeong HT. Achieving high strength and high ductility in magnesium alloys using severe plastic deformation combined with low-temperature aging. Scripta Materialia. 2009;61:1040-3.
[129] Jamali SS, Faraji G, Abrinia K. Evaluation of mechanical and metallurgical properties of AZ91 seamless tubes produced by radial-forward extrusion method. Materials Science and Engineering: A. 2016;666:176-83.
[130] Zhang L, Wang Q, Liao W, Guo W, Ye B, Jiang H, et al. Effect of homogenization on the microstructure and mechanical properties of the repetitive-upsetting processed AZ91D alloy. Journal of Materials Science & Technology. 2017;33:935-40.
[131] Lee JU, Kim S-H, Kim YJ, Park SH. Effects of homogenization time on aging behavior and mechanical properties of AZ91 alloy. Materials Science and Engineering: A. 2018;714:49-58.
[132] Nussbaum G, Sainfort P, Regazzoni G, Gjestland H. Strengthening mechanisms in the rapidly solidified AZ 91 magnesium alloy. Scripta Metallurgica. 1989;23:1079-84.
[133] Ono N, Nowak R, Miura S. Effect of deformation temperature on Hall–Petch relationship registered for polycrystalline magnesium. Materials Letters. 2004;58:39-43.
[134] Barnett MR, Keshavarz Z, Beer AG, Atwell D. Influence of grain size on the compressive deformation of wrought Mg–3Al–1Zn. Acta Materialia. 2004;52:5093-103.
[135] Atwell DL, Barnett MR, Hutchinson WB. The effect of initial grain size and temperature on the tensile properties of magnesium alloy AZ31 sheet. Materials Science and Engineering: A. 2012;549:1-6.
[136] Langdon TG. Seventy-five years of superplasticity: historic developments and new opportunities. Journal of Materials Science. 2009;44:5998.
[137] Figueiredo RB, Langdon TG. Developing superplasticity in a magnesium AZ31 alloy by ECAP. Journal of Materials Science. 2008;43:7366-71.
[138] Figueiredo RB, Langdon TG. Evaluating the superplastic flow of a magnesium AZ31 alloy processed by equal-channel angular pressing. Metallurgical and Materials Transactions A. 2014;45:3197-204.

[139] Kawasaki M, Balasubramanian N, Langdon TG. Flow mechanisms in ultrafine-grained metals with an emphasis on superplasticity. Materials Science and Engineering: A. 2011;528:6624-9.
[140] Figueiredo RB, Langdon TG. Analysis of the creep behavior of fine-grained AZ31 magnesium alloy. Materials Science and Engineering: A. 2020;787:139489.
[141] Figueiredo RB, Langdon TG. Using high-pressure torsion to achieve superplasticity in an AZ91 magnesium alloy. Metals. 2020;10:681.
[142] Kawasaki M, Langdon TG. The contribution of severe plastic deformation to research on superplasticity. Materials Transactions. 2019;60:1123-30.
[143] Kawasaki M, Langdon TG. Review: achieving superplastic properties in ultrafine-grained materials at high temperatures. Journal of Materials Science. 2016;51:19-32.
[144] Kawasaki M, Langdon TG. Principles of superplasticity in ultrafine-grained materials. Journal of Materials Science. 2007;42:1782-96.
[145] Ishikawa H, Mohamed FA, Langdon TG. The influence of strain rate on ductility in the superplastic Zn–22% Al eutectoid. The Philosophical Magazine. 1975;32:1269-71.
[146] Mohamed FA, Ahmed MMI, Langdon TG. Factors influencing ductility in the superplastic Zn-22 Pct Al eutectoid. Metallurgical Transactions A. 1977;8:933-8.
[147] Li Y, Langdon TG. A simple procedure for estimating threshold stresses in the creep of metal matrix composites. Scripta Materialia. 1997;36:1457-60.
[148] Li Y, Langdon TG. A unified interpretation of threshold stresses in the creep and high strain rate superplasticity of metal matrix composites. Acta Materialia. 1999;47:3395-403.
[149] Chaudhury PK, Sivaramakrishnan V, Mohamed FA. Superplastic deformation behavior in commercial and high purity Zn- 22 Pct Al. Metallurgical Transactions A. 1988;19:2741-52.
[150] Chaudhury PK, Mohamed FA. Effect of impurity content on superplastic flow in the Zn-22% Al alloy. Acta Metallurgica. 1988;36:1099-110.
[151] Langdon TG. An evaluation of the strain contributed by grain boundary sliding in superplasticity. Materials Science and Engineering: A. 1994;174:225-30.
[152] Taleff EM, Henshall GA, Nieh TG, Lesuer DR, Wadsworth J. Warm-temperature tensile ductility in Al−Mg alloys. Metallurgical and Materials Transactions A. 1998;29:1081-91.
[153] Taleff EM, Lesuer DR, Wadsworth J. Enhanced ductility in coarse-grained Al-Mg alloys. Metallurgical and Materials Transactions A. 1996;27:343-52.
[154] Krajewski PE, Schroth JG. Overview of quick plastic forming technology. Materials Science Forum. 2007;551-552:3-12.
[155] Langdon TG. The background to superplastic forming and opportunities arising from new developments. Solid State Phenomena. 2020;306:1-8.
[156] Valiev RZ, Salimonenko DA, Tsenev NK, Berbon PB, Langdon TG. Observations of high strain rate superplasticity in commercial aluminum alloys with ultrafine grain sizes. Scripta Materialia. 1997;37:1945-50.
[157] Horita Z, Furukawa M, Nemoto M, Barnes AJ, Langdon TG. Superplastic forming at high strain rates after severe plastic deformation. Acta Materialia. 2000;48:3633-40.
[158] Barnes AJ. Superplastic forming 40 years and still growing. Journal of Materials Engineering and Performance. 2007;16:440-54.
[159] Lin HK, Huang JC, Langdon TG. Relationship between texture and low temperature superplasticity in an extruded AZ31 Mg alloy processed by ECAP. Materials Science and Engineering: A. 2005;402:250-7.

[160] Xu J, Wang XW, Shirooyeh M, Xing GN, Shan DB, Guo B, et al. Microhardness, microstructure and tensile behavior of an AZ31 magnesium alloy processed by high-pressure torsion. Journal of Materials Science. 2015;50:7424-36.
[161] Figueiredo RB, Langdon TG. Grain refinement and mechanical behavior of a magnesium alloy processed by ECAP. Journal of Materials Science. 2010;45:4827-36.
[162] Figueiredo RB, Pereira PHR, Langdon TG. Low temperature superplasticity in ultrafine-grained AZ31 alloy. Defect and Diffusion Forum. 2018;385:59-64.
[163] Figueiredo RB, Langdon TG. Achieving superplastic properties in a ZK10 magnesium alloy processed by equal-channel angular pressing. Journal of Materials Research and Technology. 2016.
[164] Malheiros LRC, Figueiredo RB, Langdon TG. Grain size and microhardness evolution during annealing of a magnesium alloy processed by high-pressure torsion. Journal of Materials Research and Technology. 2015;4:14-7.
[165] Neishi K, Horita Z, Langdon TG. Achieving superplasticity in ultrafine-grained copper: influence of Zn and Zr additions. Materials Science and Engineering: A. 2003;352:129-35.
[166] Batista BA, Soares RB, Lins VFC, Figueiredo RB, Hohenwarter A, Matencio T. Corrosion in Hank's solution and mechanical strength of ultrafine-grained pure iron. Advanced Engineering Materials.n/a:2000183.
[167] Matsumura N, Tokizane M. Austenite grain refinement and superplasticity in niobium microalloyed steel. Transactions of the Iron and Steel Institute of Japan. 1986;26:315-21.
[168] Figueiredo RB, Langdon TG. Strategies for achieving high strain rate superplasticity in magnesium alloys processed by equal-channel angular pressing. Scripta Materialia. 2009;61:84-7.
[169] Chong Y, Deng G, Gao S, Yi J, Shibata A, Tsuji N. Yielding nature and Hall-Petch relationships in Ti-6Al-4V alloy with fully equiaxed and bimodal microstructures. Scripta Materialia. 2019;172:77-82.
[170] Demirtas M, Purcek G, Yanar H, Zhang ZJ, Zhang ZF. Achieving room temperature superplasticity in Zn–5Al alloy at high strain rates by equal-channel angular extrusion. Journal of Alloys and Compounds. 2015;623:213-8.
[171] Demirtas M, Purcek G, Yanar H, Zhang ZJ, Zhang ZF. Effect of equal-channel angular pressing on room temperature superplasticity of quasi-single phase Zn–0.3Al alloy. Materials Science and Engineering: A. 2015;644:17-24.
[172] Málek P, Lukáč P. Superplasticity in A Zn-1·1 wt. % Al alloy. Czechoslovak Journal of Physics B. 1986;36:498-508.
[173] Wu X, Zhu Y, Lu K. Ductility and strain hardening in gradient and lamellar structured materials. Scripta Materialia. 2020;186:321-5.
[174] Chinh NQ, Valiev RZ, Sauvage X, Varga G, Havancsák K, Kawasaki M, et al. Grain boundary phenomena in an ultrafine-grained Al–Zn alloy with improved mechanical behavior for micro-devices. Advanced Engineering Materials. 2014;16:1000-9.
[175] Sauvage X, Duchaussoy A, Zaher G. Strain induced segregations in severely deformed materials. Materials Transactions. 2019;60:1151-8.
[176] Sun WT, Qiao XG, Zheng MY, Zhao XJ, Chen HW, Gao N, et al. Achieving ultra-high hardness of nanostructured Mg-8.2Gd-3.2Y-1.0Zn-0.4Zr alloy produced by a combination of high pressure torsion and ageing treatment. Scripta Materialia. 2018;155:21-5.

[177] Horky J, Ghaffar A, Werbach K, Mingler B, Pogatscher S, Schaublin R, et al. Exceptional strengthening of biodegradable Mg-Zn-Ca alloys through high pressure torsion and subsequent heat treatment. Materials. 2019;12.
[178] Basha DA, Sahara R, Somekawa H, Rosalie JM, Singh A, Tsuchiya K. Interfacial segregation induced by severe plastic deformation in a Mg–Zn–Y alloy. Scripta Materialia. 2016;124:169-73.
[179] Sha G, Yao L, Liao X, Ringer SP, Chao Duan Z, Langdon TG. Segregation of solute elements at grain boundaries in an ultrafine grained Al–Zn–Mg–Cu alloy. Ultramicroscopy. 2011;111:500-5.
[180] Sauvage X, Enikeev N, Valiev R, Nasedkina Y, Murashkin M. Atomic-scale analysis of the segregation and precipitation mechanisms in a severely deformed Al–Mg alloy. Acta Materialia. 2014;72:125-36.

Figure captions:

Figure 1 – Illustration of the deformation mechanism.

Figure 2 – Flow stress plotted as a function of grain size for different metals. Experimental data for Al [35-41], Cu [18, 22, 42-51], Fe [52-58] and Ni [14, 59-62] are also included.

Figure 3 – Predicted flow stress as a function of grain size for Al, Cu, Fe and Mg.

Figure 4 – Stress as a function of grain size for copper deformed at different temperatures.

Figure 5 – Flow stress plotted as a function of grain size for magnesium tested at room temperature. Experimental data [15, 23, 80, 84] are also shown.

Figure 6 – Prediction of stress vs grain size for pure zinc and experimental data for a Zn-22% Al alloy [86].

Figure 7 – Strain rate sensitivity, m, plotted as a function of stress for copper. Experimental data [46, 87] are also plotted.

Figure 8 – Flow stress plotted as a function of strain rate for (a) zinc and (b) aluminum. Experimental data [29, 91] are also shown.

Figure 9 – Flow stress plotted as a function of the inverse of the square root of the grain size for (a) iron, (b) titanium and (c) aluminum. Experimental data for Fe [52-57, 94, 95], Ti (grades 1, 2 and 3) and Ti-6Al-4V [96-114], Al [35-41] and Al-Mg [115-117] are also plotted.

Figure 10 – Flow stress of magnesium with a threshold stress plotted as a function of (a) the grain size and (b) the strain rate. Experimental data for the AZ91 alloy [123-132] is also shown.

Figure 11 – Flow stress plotted as a function of the inverse of the square root of the grain size of γ-Fe at different temperatures. Experimental data for 316L austenitic stainless steel [95] are also plotted.

Figure 12 – Flow stress plotted as a function of the inverse of the square root of the grain size of Mg at different temperatures. Experimental data for AZ31 alloy [134] are also shown.

Figure 13 – (a) Flow stress and (b) strain-rate sensitivity plotted as a function of the strain rate for aluminum tested at different temperatures. Experimental data for an Al-Mg-Sc alloy [118] is also shown.

Figure 14 – Flow stress and strain rate sensitivity plotted as a function of strain rate for magnesium at 423 K. Experimental data for the AZ31 alloy [160, 162] are also shown for comparison.

Figure 15 – Flow stress determined experimentally plotted as a function of the predictions by the model for different materials. Experimental data for Al [29, 35-41, 115, 116, 118], Cu [18, 22, 42-51, 165], Fe (α) [52-58, 166], Fe (α+γ) [167], Fe (γ) [94, 95], Mg [23, 123, 133-135, 137, 140, 141, 159, 160, 162, 168], Ni [14, 59-62], Ti [96-114, 169] and Zn [86, 91, 170-172].

Declaration of interests

☒ The authors declare that they have no known competing financial interests or personal relationships that could have appeared to influence the work reported in this paper.

☐The authors declare the following financial interests/personal relationships which may be considered as potential competing interests:

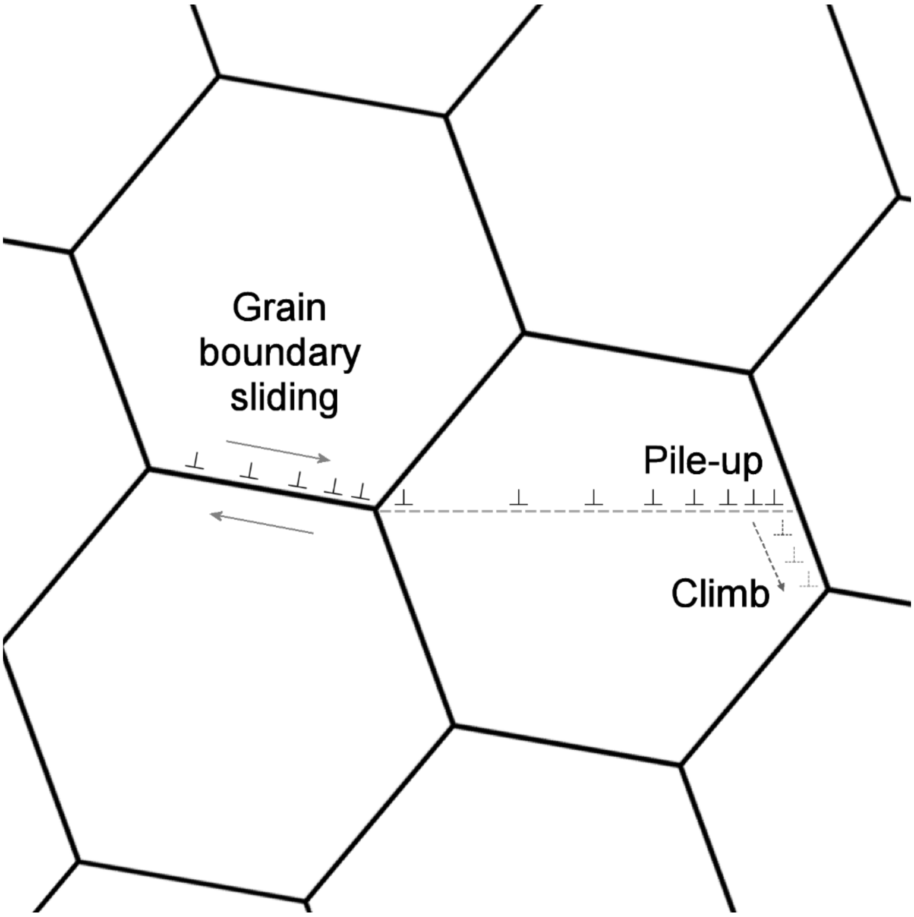

Figure 1 – Illustration of the deformation mechanism.

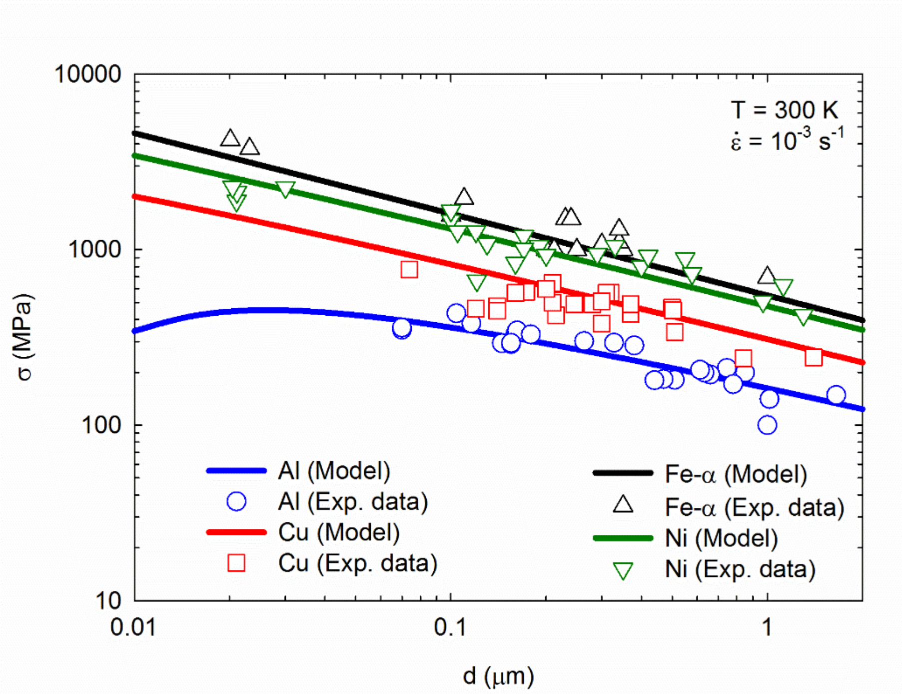

Figure 2 – Flow stress plotted as a function of grain size for different metals. Experimental data for Al [35-41], Cu [18, 22, 42-51], Fe [52-58] and Ni [14, 59-62] are also included.

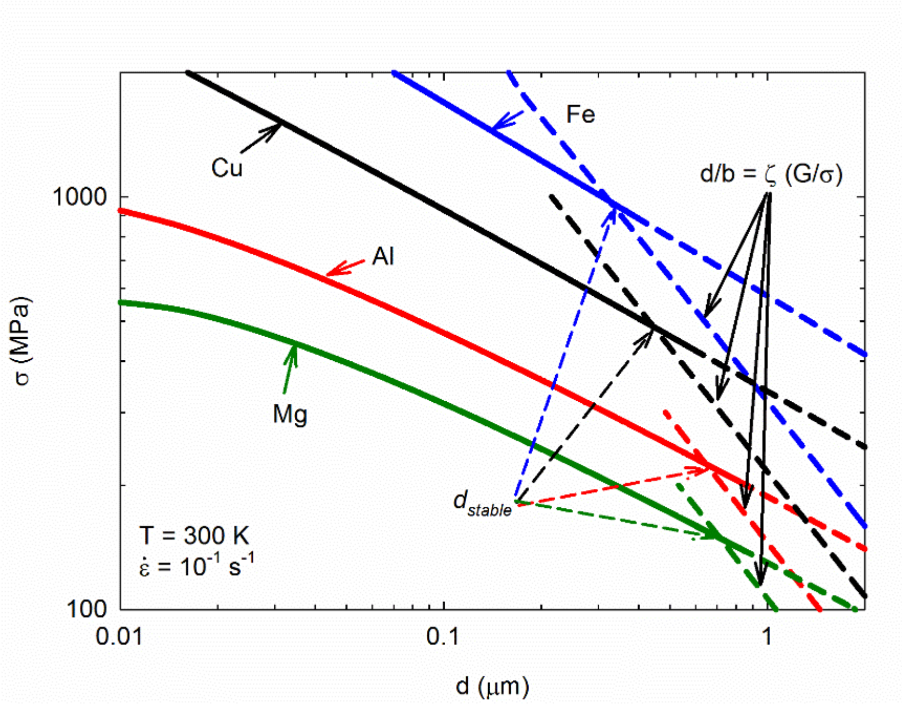

Figure 3 – Predicted flow stress as a function of grain size for Al, Cu, Fe and Mg.

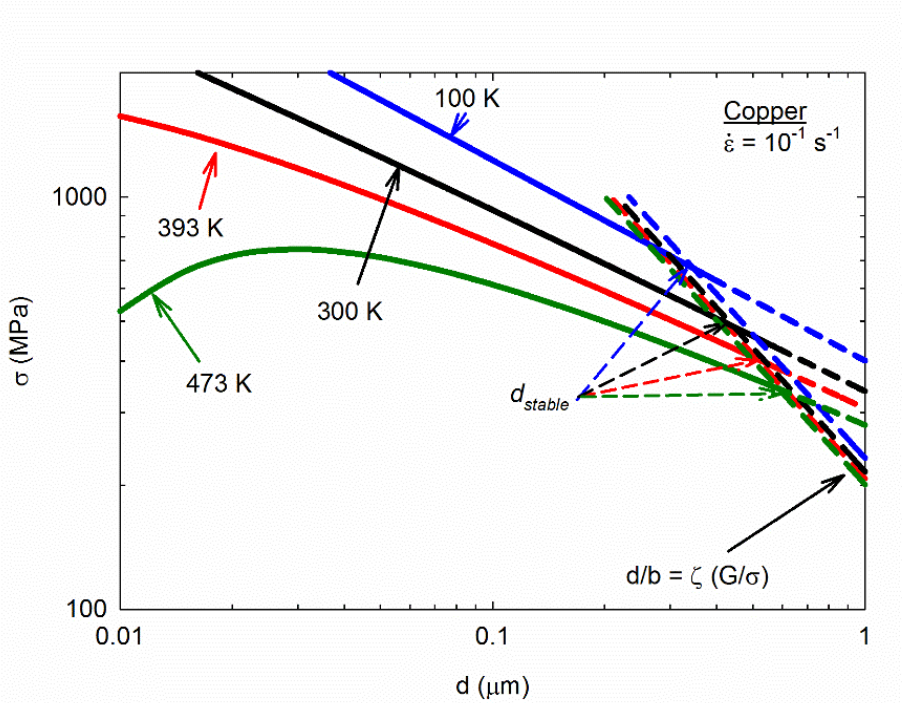

Figure 4 – Stress as a function of grain size for copper deformed at different temperatures.

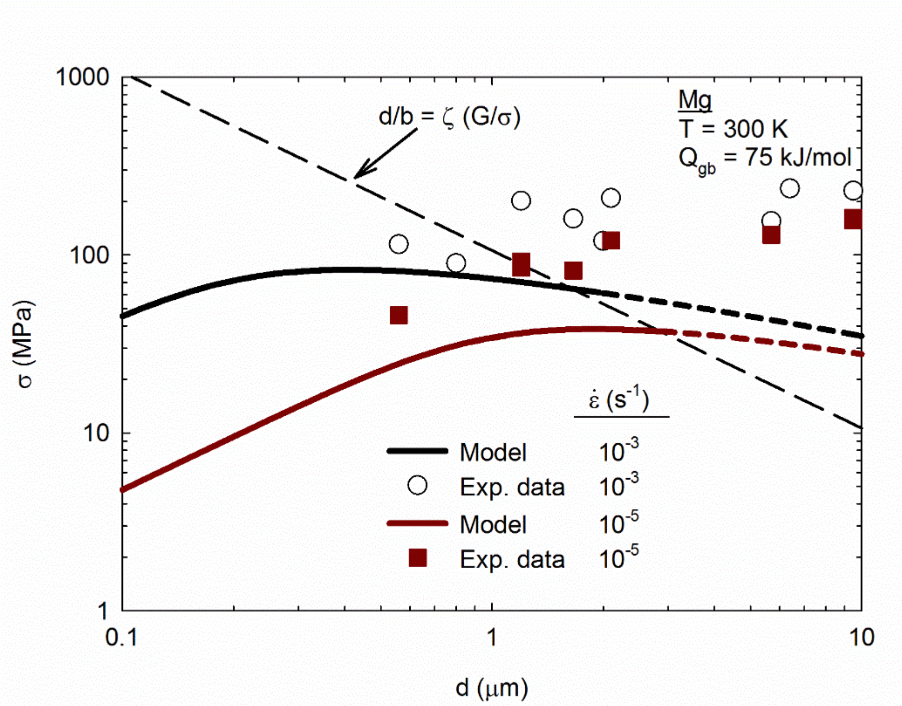

Figure 5 – Flow stress plotted as a function of grain size for magnesium tested at room temperature. Experimental data [15, 23, 80, 84] are also shown.

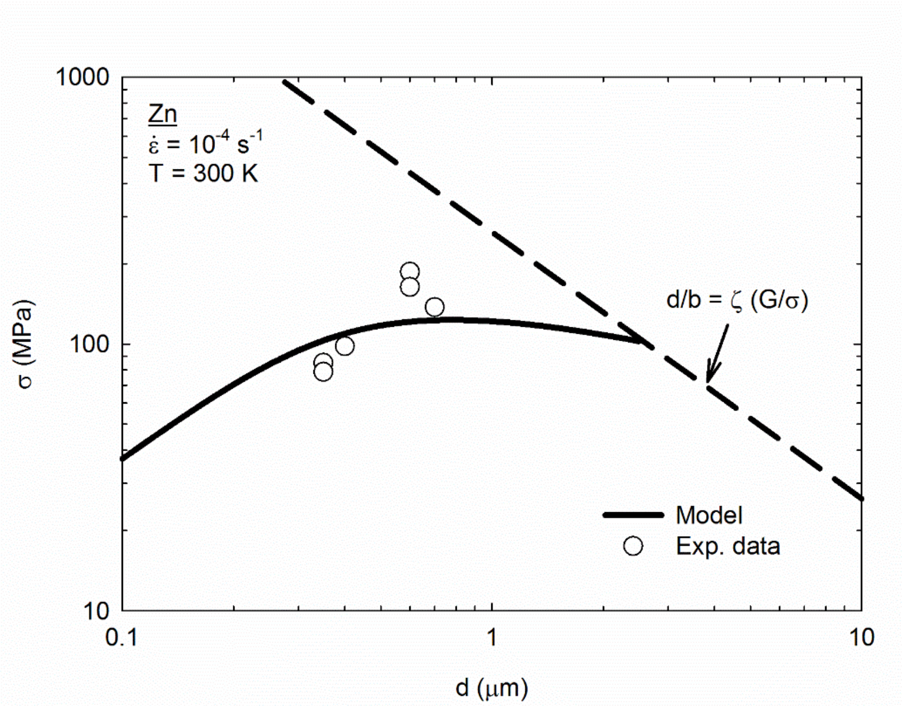

Figure 6 – Prediction of stress vs grain size for pure zinc and experimental data for a Zn-22% Al alloy [86].

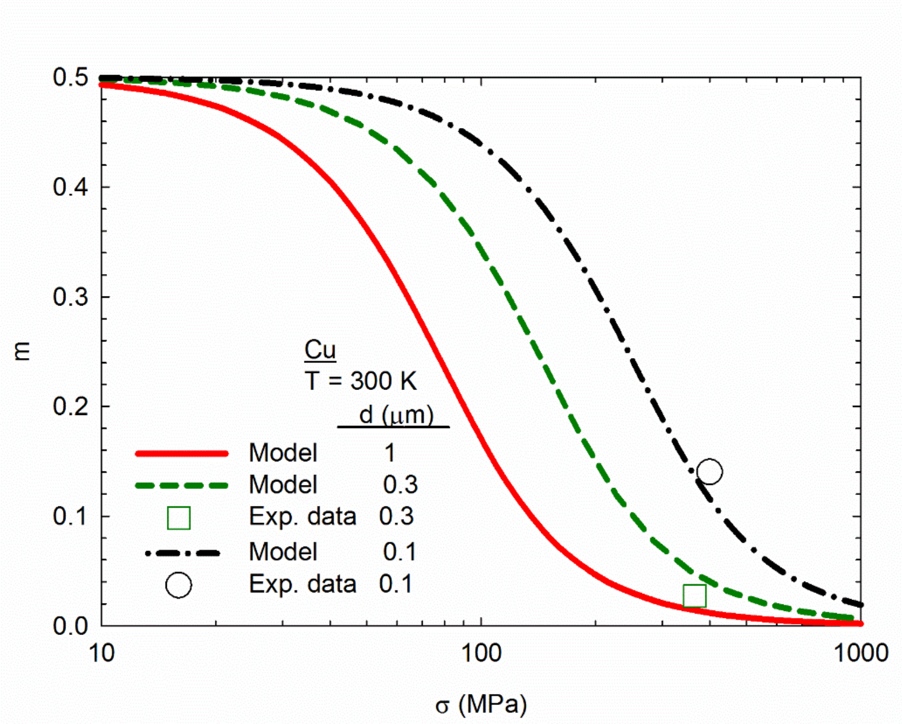

Figure 7 – Strain rate sensitivity, m, plotted as a function of stress for copper. Experimental data [46, 87] are also plotted.

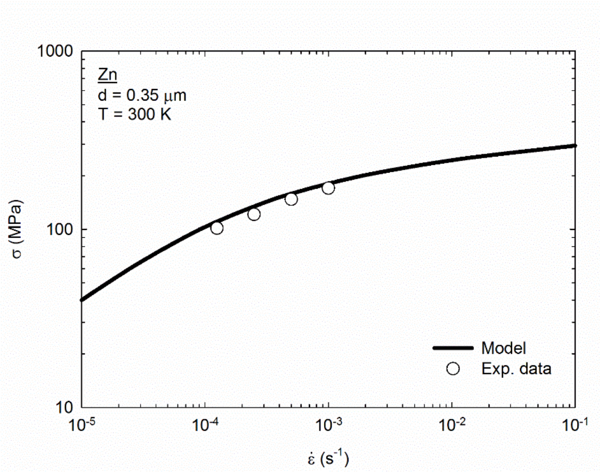

(a)

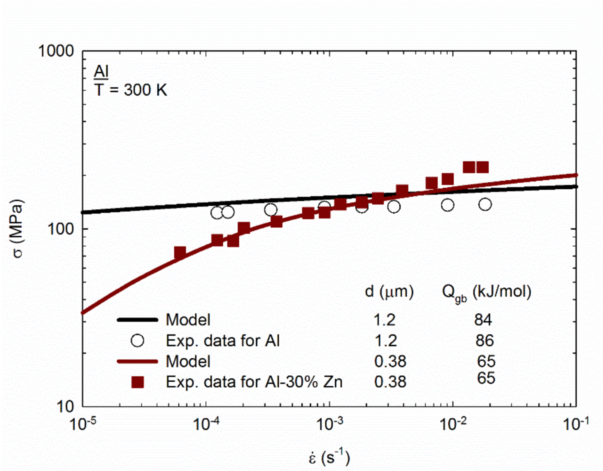

(b)

Figure 8 – Flow stress plotted as a function of strain rate for (a) zinc and (b) aluminum.

Experimental data [29, 91] are also shown.

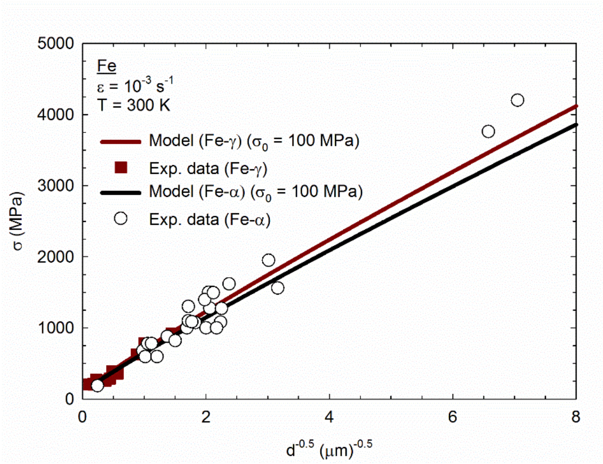

(a)

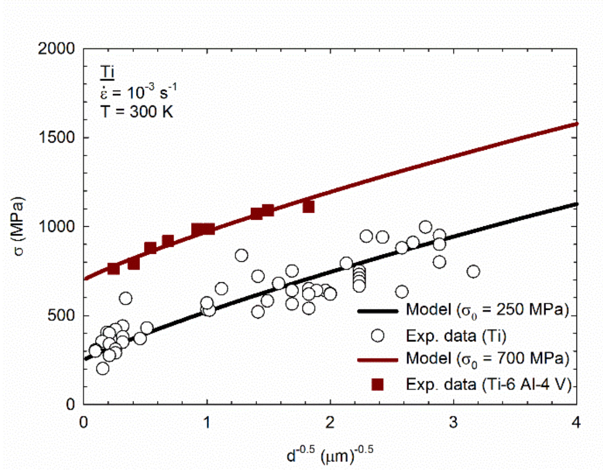

(b)

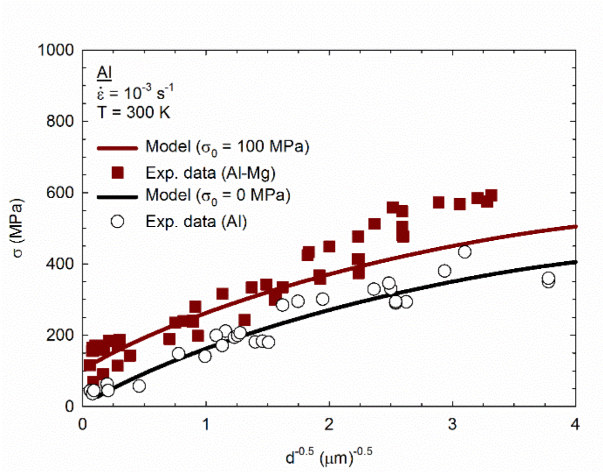

(c)

Figure 9 – Flow stress plotted as a function of the inverse of the square root of the grain size for (a) iron, (b) titanium and (c) aluminum. Experimental data for Fe [52-57, 94, 95], Ti (grades 1, 2 and 3) and Ti-6Al-4V [96-114], Al [35-41] and Al-Mg [115-117] are also plotted.

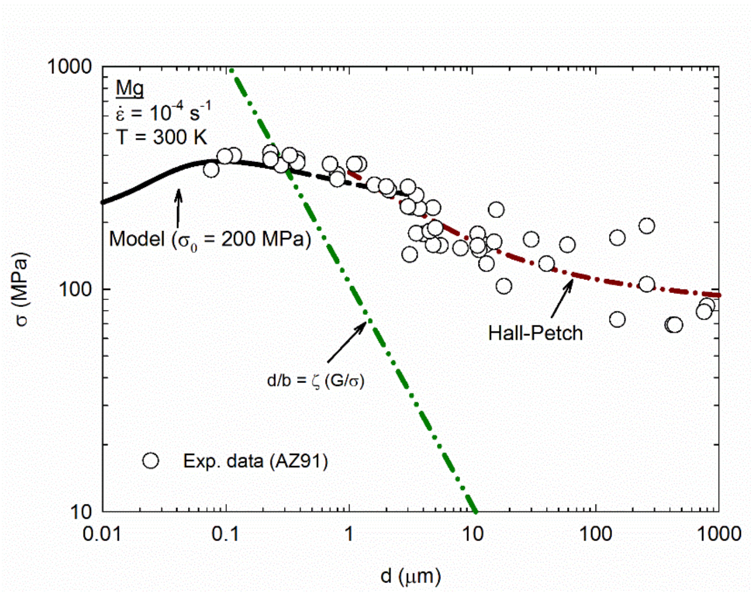

(a)

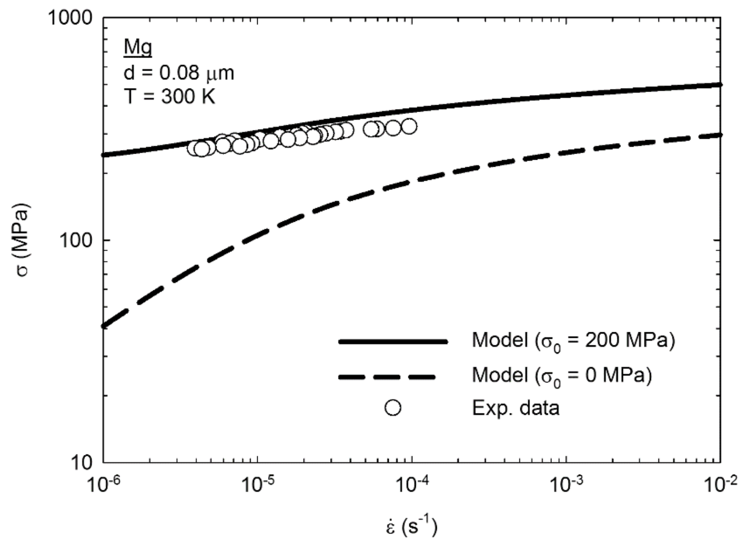

(b)

Figure 10 – Flow stress of magnesium with a threshold stress plotted as a function of (a) the grain size and (b) the strain rate. Experimental data for the AZ91 alloy [123-132] is also shown.

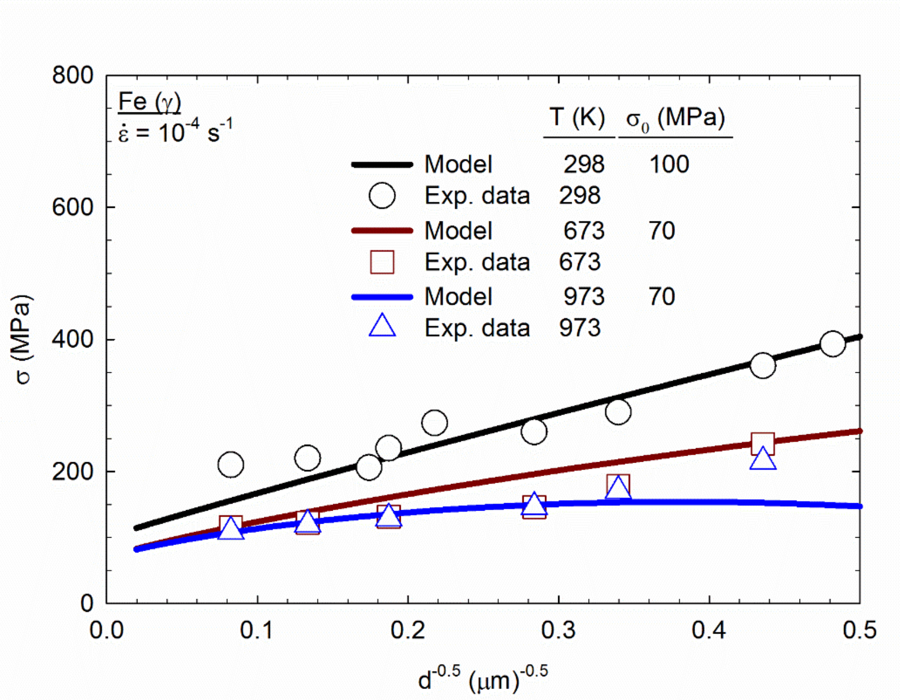

Figure 11 – Flow stress plotted as a function of the inverse of the square root of the grain size of γ-Fe at different temperatures. Experimental data for 316L austenitic stainless steel [95] are also plotted.

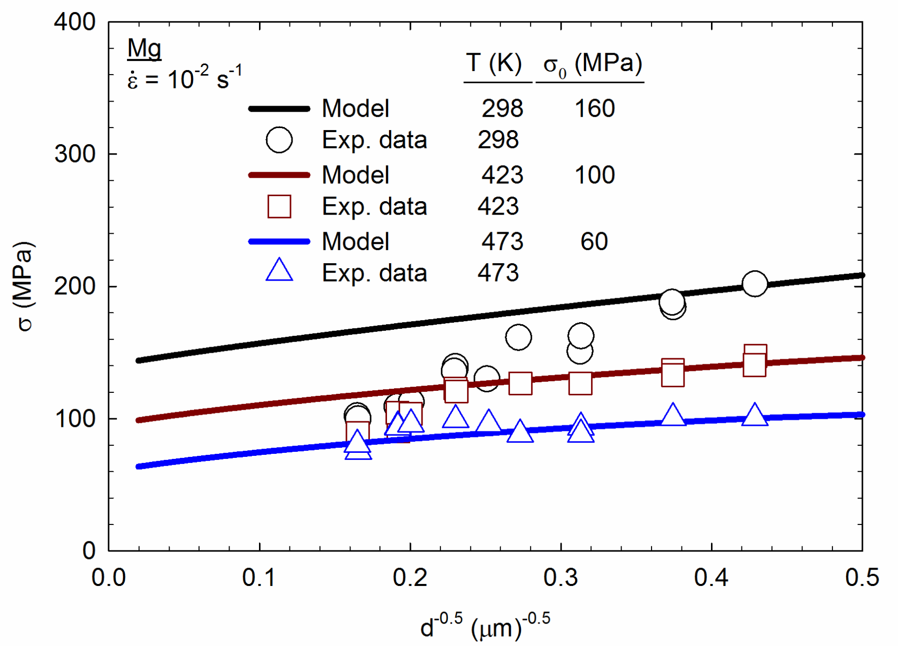

Figure 12 – Flow stress plotted as a function of the inverse of the square root of the grain size of Mg at different temperatures. Experimental data for AZ31 alloy [134] are also shown.

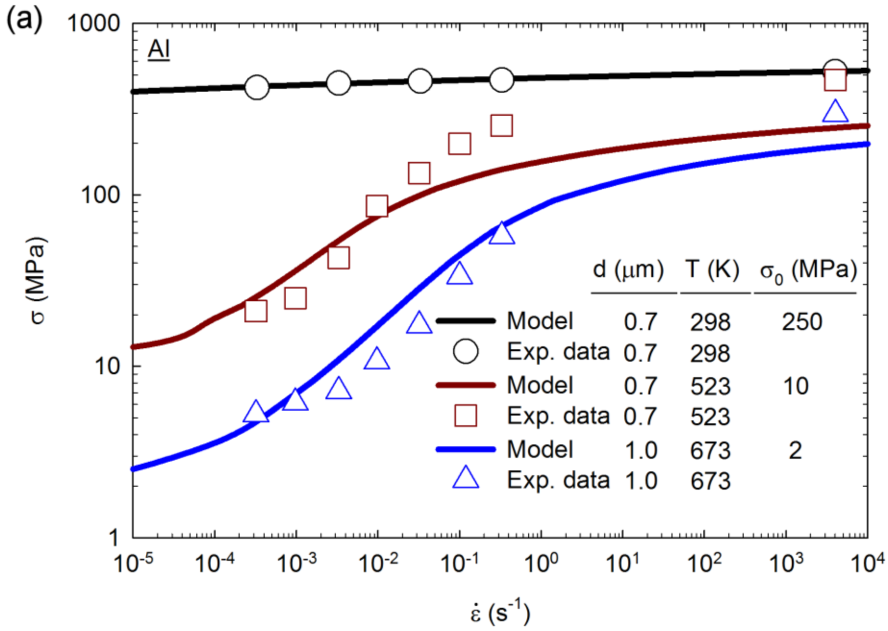

Figure 13 – (a) Flow stress and (b) strain-rate sensitivity plotted as a function of the strain rate for aluminum tested at different temperatures. Experimental data for an Al-Mg-Sc alloy [118] is also shown.

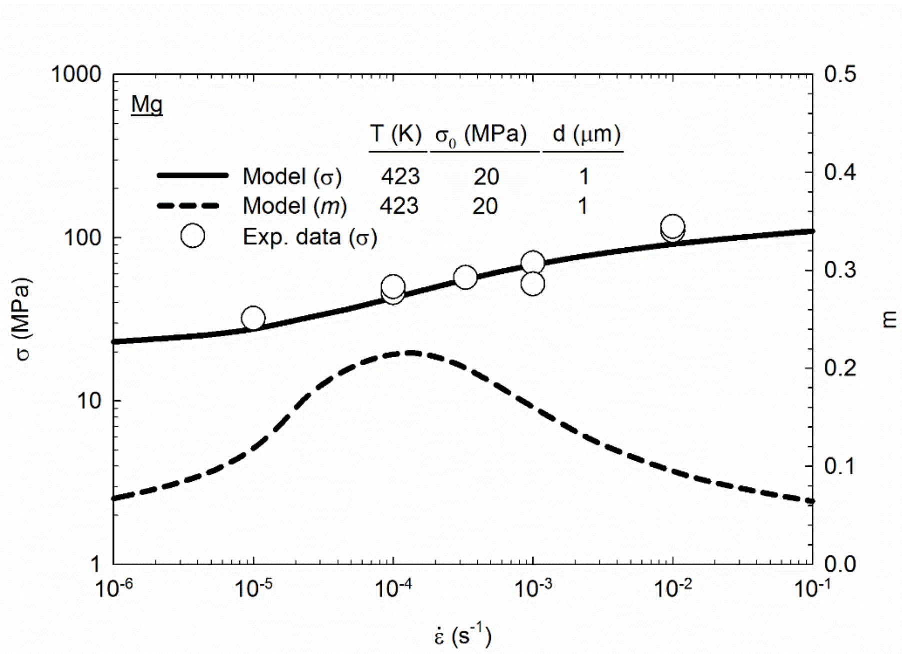

Figure 14 – Flow stress and strain rate sensitivity plotted as a function of strain rate for magnesium at 423 K. Experimental data for the AZ31 alloy [160, 162] are also shown for comparison.

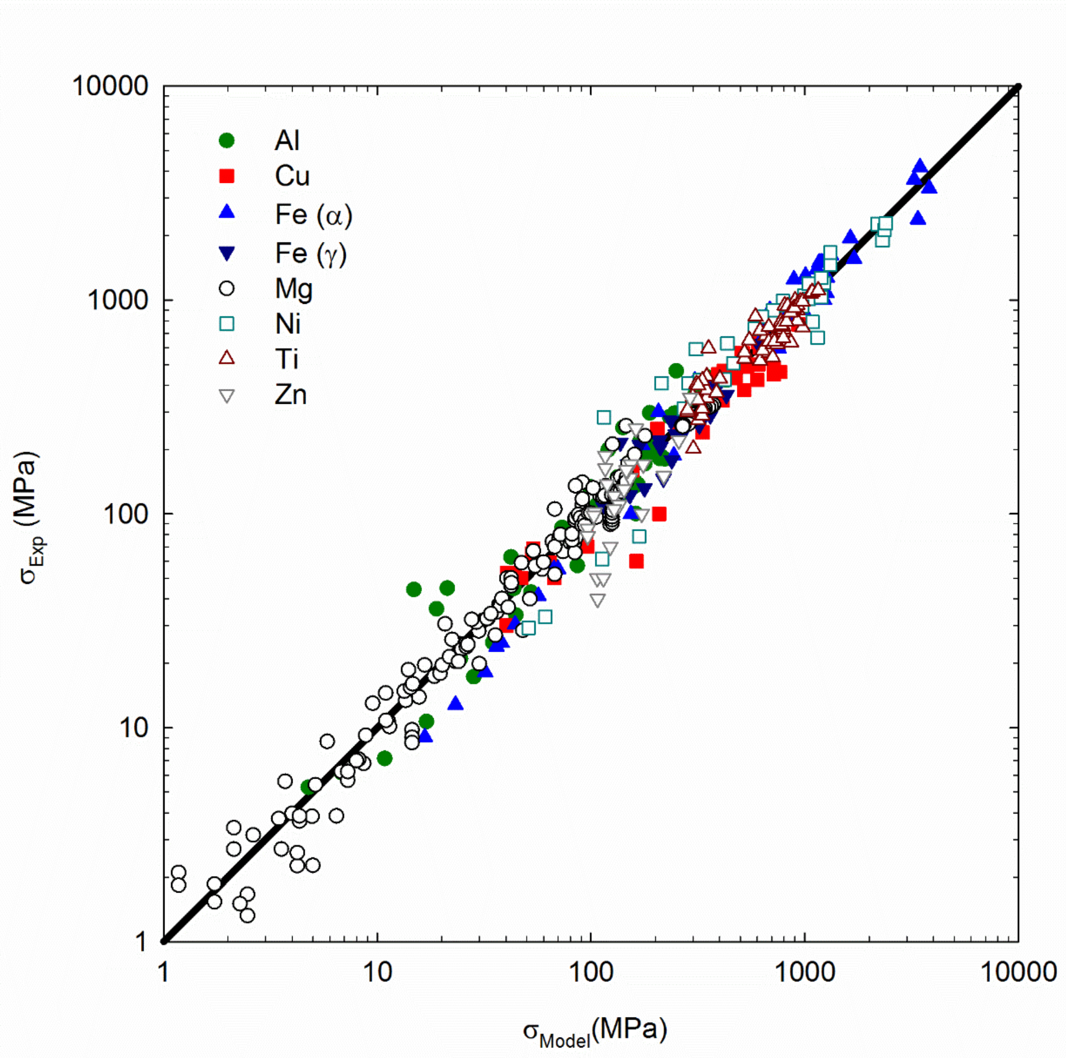

Figure 15 – Flow stress determined experimentally plotted as a function of the predictions by the model for different materials. Experimental data for Al [29, 35-41, 115, 116, 118], Cu [18, 22, 42-51, 165], Fe (α) [52-58, 166], Fe (α+γ) [167], Fe (γ) [94, 95], Mg [23, 123, 133-135, 137, 140, 141, 159, 160, 162, 168], Ni [14, 59-62], Ti [96-114, 169] and Zn [86, 91, 170-172].

Table 1 – Summary of parameters used in the model.

Material	b (nm)	G (MPa) *	Grain boundary diffusion	
			δD_0 (m^3/s)	Q_{gb} (kJ/mol)
Aluminum	0.286	29500 – 13.6 × T	5×10^{-14}	84**
Copper	0.256	47100 – 16.7 × T	5×10^{-15}	104
Iron (α)	0.248	72600 – 28.7 × T	1.1×10^{-12}	174
Iron (γ)	0.258	93200 – 40.7 × T	7.5×10^{-14}	159
Magnesium	0.320	19200 – 8.8 × T	5×10^{-12}	92**
Nickel	0.249	87700 – 29.3 × T	3.5×10^{-15}	115
Titanium (α)	0.295	51700 – 27.0 × T	3.6×10^{-16}	97
Zinc	0.267	60000 – 35.6 × T	1.3×10^{-14}	60.5

* considering T as the absolute temperature in K.

** values of activation energy determined in experiments were also considered.

Table 2 – Summary of experimental data used to validate the model.

Material	d (μm)	T (K)	$\dot{\varepsilon}$ (s^{-1})	Type of test	σ_0 (MPa)	Ref.
Al	0.2 ~ 15	300	8.3×10^{-4}	Tension / Hardness	-	Tsuji *et al.* [35]
Al	0.16/ 0.38	300	10^{-4}	Hardness	-	Edalati *et al.* [36]
Al	0.6 ~ 23	300	3.3×10^{-4}	Tension	-	Horita *et al.* [37]
Al	0.104 ~ 1	300	10^{-4}	Hardness	-	Bachmaier and Pippan [38]
Al	0.44 ~ 0.78	300	10^{-3}	Tension	-	Chen *et al.* [39]
Al	0.116 ~ 0.179	300	10^{-3}	Tension	-	Haves *et al.* [40]
Al-GNP	0.07/ 0.155	300	10^{-3}	Tension/ Hardness	-	Huang *et al.* [41]
Al	1.2	300	10^{-4} ~ 2×10^{-2}	Dynamic hardness	-	Chinh *et al.* [29]
Al-Zn	0.38	300	6×10^{-5} ~ 2×10^{-2}	Dynamic hardness	-	Chinh *et al.* [29]
Al-Mg	0.1 ~ 170	300	10^{-4}	Hardness	100	Furukawa *et al.* [115]
Al-Mg	0.2 ~ 300	300	4×10^{-4}	Tension	100	Hayes *et al.* [116]
Al-Mg-Sc	0.7 ~ 1.0	298 / 523 / 673	3.3×10^{-4} ~ 4×10^{3}	Tension / Compression	2 / 10 / 250	Pereira *et al.* [118]
Cu	0.37	300	10^{-4}	Hardness	-	Valiev *et al.* [18]

Cu-CNT / Cu	0.074 / 0.173	300	10^{-4}	Hardness	-	Jenei *et al.* [42]
Cu	0.16 / 0.215	300	10^{-4}	Hardness	-	Gubicza *et al.* [43]
Cu	0.31	300	10^{-4}	Hardness	-	Zhilyaev *et al.* [44]
Cu	0.28 / 0.37	300	10^{-4}	Hardness	-	Almazrouee *et al.* [45]
Cu	0.21 ~ 0.5	300	10^{-4}	Tension	-	Wang and Ma [46]
Cu	0.14	300	10^{-4}	Hardness	-	Horita and Langdon [47]
Cu	0.14	300	10^{-4}	Hardness	-	An *et al.* [48]
Cu	0.21/ 30	300	10^{-3}	Compression	-	Valiev *et al.* [22]
Cu	5.6 ~ 88	300	3×10^{-4}	Tension	-	Flinn *et al.* [49]
Cu	0.2 ~ 4.2	300	8.3×10^{-4}	Tension	-	Tian *et al.* [50]
Cu	0.24 ~ 1.4	300	10^{-4}	Hardness	-	Schafler and Kerber [51]
Cu-Zn-Zr	1	673	10^{-4} ~ 10^{-1}	Tension	-	Neishi *et al.* [165]
Fe (α)	0.2	300	10^{-4}	Hardness	100	Edalati *et al.* [52]
Fe (α)	0.25	300	10^{-4}	Hardness	100	Wetscher *et al.* [53]
Fe (α)	0.1	300	10^{-4}	Hardness	100	Valiev *et al.* [54]
Fe (α)	0.3 ~ 5	300	10^{-4}	Hardness	100	Hohenwarter *et al.* [55]

Fe (α)	0.36 / 70	300	5.5×10^{-4}	Tension	100	Muñoz *et al.* [56]
Fe (α)	0.11 ~ 140	300	3.3×10^{-3}	Tension / Hardness	100	Tejedor *et al.* [57]
Fe (α)	~0.02	300	10^{-4}	Hardness	100	Borchers *et al.* [58]
Fe (α)	0.46 ~ 8.0	300	10^{-3}	Compression	100	Batista *et al.* [166]
Fe (α+γ)	5	1063	2.4×10^{-5} ~1×10^{-3}	Tension	-	Matsumura and Tokizane [167]
Fe (γ)	3 ~ 87	298 ~ 973	10^{-4}	Tension	100 / 70	Kashyap and Tangri [95]
Fe (γ)	0.5 ~ 33	300	10^{-4}	Tension	100	Takaki *et al.* [94]
Mg	0.5	300	10^{-5} ~ 10^{-1}	Tension	20	Figueiredo *et al.* [23]
Mg	43 ~ 172	423 / 473 / 523	1.7×10^{-4}	Tension	20 / 10 / 0	Ono *et al.* [133]
Mg (AZ91 + Al_2O_3)	0.08	300	4×10^{-6} ~ 1×10^{-4}	Dynamic hardness	200	Castro *et al.* [123]
Mg (AZ91)	1.3 ~ 9.6	423 / 523 / 623	1×10^{-5} ~ 1×10^{-1}	Tension	10 / 0 / 0	Figueiredo and Langdon [141]

Mg (AZ31)	12 ~ 27	573 / 623 / 673	$5.8 \times 10^{-7} \sim 3.6 \times 10^{-4}$	Double shear creep	-	Figueiredo and Langdon [140]
Mg (AZ31)	10.3	623 / 673	$3.3 \times 10^{-5} \sim 10^{-3}$	Tension	-	Figueiredo and Langdon [137]
Mg (AZ31)	1 *	423	$10^{-4} \sim 10^{-2}$	Tension	20	Xu *et al.* [160]
Mg (AZ31)	1 *	423	$10^{-5} \sim 10^{-2}$	Tension	20	Figueiredo *et al.* [162]
Mg (AZ31)	1	423	$10^{-4} \sim 10^{-2}$	Tension	20	Lin *et al.* [159]
Mg (AZ31)	4.9 ~ 80	298/ 393/ 453/ 513	10^{-3}	Tension	120/ 100/ 70/ 60	Atwell *et al.* [135]
Mg (AZ31)	5.4 ~ 37	423/ 473	10^{-2}	Compression	100/ 60	Barnett *et al.* [134]
Mg (ZK60)	~1.4	450/ 473/ 513	$10^{-5} \sim 10^{-2}$	Tension	-	Figueiredo and Langdon [168]
Ni	0.2 ~ 5.9	300	10^{-4}	Hardness	-	Zhang *et al.* [59]
Ni	0.03 ~ 0.2	300	10^{-4}	Hardness	-	Bachmaier *et al.* [60]
Ni	0.021 / 0.105	300	5×10^{-5}	Tension	-	Dalla Torre *et al.* [61]
Ni	0.12 ~ 0.55	300	2×10^{-3}	Tension	-	Krasilnikov *et al.* [14]

Ni	0.02 ~ 21	300	10^{-4}	Hardness	-	Hughes *et al.* [62]
Ti	0.13/ 0.61/ 8.6	300	10^{-4}	Hardness	250	Wang *et al.* [96]
Ti	0.4/ 28	300	1.7×10^{-3}	Tension	250	Zhao *et al.* [97]
Ti	0.2 ~ 23	300	1.7×10^{-3}	Tension	250	Zhao *et al.* [98]
Ti	0.3 / 15	300	10^{-3}	Tension	250	Ko *et al.* [99]
Ti	0.12 ~ 110	300	5×10^{-4}	Tension	250	Yapici *et al.* [100]
Ti	0.19/ 0.45/ 45	300	10^{-3}	Tension	250	Stolyarov *et al.* [101]
Ti	0.96/ 41.6	300	10^{-3} *	Tension	250	Kang and Kim [102]
Ti	0.3 / 110	300	5×10^{-4}	Tension	250	Purcek *et al.* [103]
Ti	0.3 / 10	300	10^{-3}	Tension	250	Zhang *et al.* [104]
Ti	0.15 / 15	300	10^{-3}	Tension	250	Sordi *et al.* [105]
Ti	0.2/ 0.3/ 10	300	10^{-3} *	Tension	250	Stolyarov *et al.* [106]
Ti	0.12	300	10^{-3}	Tension	250	Sergueeva *et al.* [107]
Ti	0.26 ~ 10	300	10^{-3}	Tension	250	Stolyarov *et al.* [108]
Ti	0.12	300	3.3×10^{-3}	Tension	250	Stolyarov *et al.* [109]
Ti	0.17/ 0.28	300	3.3×10^{-3}	Tension	250	Stolyarov *et al.* [110]

Ti	0.35/ 15	300	10^{-3} *	Tension	250	Sabirov *et al.* [111]
Ti	0.2 / 23	300	10^{-3} *	Tension/ Compression	250	Figueiredo *et al.* [112]
Ti	0.1 ~ 1	300	10^{-4}	Hardness	250	Salishchev *et al.* [113]
Ti	0.8 ~ 4.76	300	10^{-3}	Compression	250	Luo *et al.* [114]
Ti-6Al-4V	0.3 ~ 17	300	8.3×10^{-4}	Tension	700	Chong *et al.* [169]
Zn-Al	0.35	300	$1.2 \times 10^{-4} \sim 10^{-3}$	Dynamic hardness	-	Kawasaki *et al.* [91]
Zn-Al	0.35 ~ 0.7	300	10^{-4}	Hardness	-	Kawasaki *et al.* [86]
Zn-Al	0.54	300	$10^{-4} \sim 10^{0}$	Tension	-	Dermirtas *et al.* [170]
Zn-Al	2	300	$10^{-4} \sim 10^{-1}$	Tension	-	Dermirtas *et al.* [171]
Zn-Al	1.87	300	$8.5 \times 10^{-5} \sim 1.7 \times 10^{-2}$	Tension	-	Málek and Lukác [172]

* Estimated value